Quantification of Spin Relaxation Rates for Chiral Lead Halide Perovskites

Jan Planelles Samper

Supervisor: Dr. Prasenjit Mandal
Examiner: Prof. Dmitry Baranov

LUNDS UNIVERSITET

Master Thesis in Chemistry
Division of Chemical Physics
Lund University, Sweden
KEMR30, 60hp

Popular Science Summary

Take a look at your left hand and then your right hand. Although they look identical, if you put one on top of the other you will see that they do not match up perfectly,just like a right-hand glove cannot fit your left hand. They are mirror images of each other but not interchangeable. This property is called chirality.

Chirality can be found in nature, where for example, DNA is in its majority right-handed. This seemingly innocent property cannot be overlooked, because having "the left hand" molecule instead of the right one can have serious consequences, like the case of the Thalidomide scandal where this medicine was given to pregnant women to combat morning sickness. While "the left hand" acted as a good medicine, "the right hand" caused deformities to the fetus and miscarriages, and more than 10,000 children were born with deformities.

This property has been studied in many fields, one of them being spintronics. This word refers to the field that studies and applies the properties of the spin of an electron to make devices for carrying and sending information (such as a hard disk drive, quantum computers or even AI). Now you might be asking yourself: what is the spin of an electron? Short answer: no one really knows. Longer answer: it is a property that the electron "just has" and it can be either up or down.

So in order to make devices for spintronic applications you need a material that has most of its electrons in either its up or down form, that is how the information is sent and preserved.

In this work we want to study perovskites, a class of materials that have a particular structure that is very good for interacting with light. We want to study for how long the spin up or down information is kept when chirality is added to these materials. Perovskites are not chiral, but scientists discovered that when a chiral molecule is placed next to one, it behaves like a chiral material.
In this work we have studied chiral perovskites and how long they keep their spin up or down information, using light, because light interacts differently with the right or left hand of a material. We have shown that there is a dependency when using "right" or "left" light with these chiral perovskites and obtained the amount of time the spin up or down information is kept, giving new insights for future spintronic applications.

Abstract

Chirality is the property of an object that cannot be superimposed onto its mirror image. Chiral materials exhibit circular dichroism (CD) which can selectively populate one spin state over the other upon optical excitation, creating a spin-polarized carrier population. In chiral hybrid organic-inorganic perovskites, chirality is transferred from the organic spacer to the inorganic framework, making these materials strong candidates for spintronic applications where spin polarization can be generated optically without external magnetic fields. The spin lifetimes of these materials depends on the measurement technique and the standard helicity-difference method carries implicit assumptions that limits its physical transparency. Here we investigate the spin dynamics of (R/S/RAC-MBA)$_2$PbI$_4$ with circularly polarized transient absorption (CP-TA) and obtain the lifetimes by the hellicity-difference method and we also propose a new kinetic model to obtain the spin rate constant. Thin films were characterized by steady-state absorption and circular dichroism spectroscopy and CP-TA with 480 nm pump and $8\mu J/cm^2$ fluence for different pump-probe polarization configurations was used to study the carrier dynamics.

The spin lifetimes were obtained by the helicity-difference method and for a coupled two-population kinetic model that separates the carrier decay into its different contributions including excitonic recombination (k_r), Auger-Meitner recombination (k_A), and spin relaxation (k_s). Both methods confirm polarization-dependent dynamics and faster spin relaxation in the racemic sample than in the pure enantiomers, consistent with the chiral organic molecule prolonging spin polarization through the chiral induced spin selectivity (CISS) effect. The kinetic model yields spin lifetimes of 43-249 ps, shorter than the 136-751 ps extracted by the helicity-difference method, confirming that spin lifetime is a model-dependent quantity. These results establish new insights into the quantification of spin relaxation rates in chiral hybrid perovskites and highlight the need for standardized approaches in this rapidly growing field.

Acknowledgments

Two years ago I was finishing my Bachelor Thesis here in Lund after deciding to stay a bit longer in Sweden. These last two years have been a truly enriching experience filled with so many moments, challenges and learnings. It is through the support and encouragement of many people that I decided to stay in Sweden, and it is many people that have made this Master Thesis possible. Because science is always a collective journey.

I would like to start by thanking Prof. Dmitry Baranov. Thank you for giving me this opportunity and letting me dive into the world of perovskites and spectroscopy, and for all the support and trust given over the last year. I am incredibly grateful for all the scientific and non-scientific advice and the mentorship provided. I hope we can stay in touch during my future career.

Many thanks to Dr. Prasenjit Mandal, with whom I have worked closely. Thank you for all your guidance when I started this project, for the synthesis and sample preparation, as well as the long days in Millenia. To Dr. Sankaran Ramesh, who introduced me to the world of ultrafast spectroscopy and has been an amazing teacher whose patience and deep knowledge have been so precious. I wish you the best in your future scientific career. To the "Italian mafia": Gioele and Lorenzo, who from the beginning gave me such a warm welcome in the division. To the uncountable hours in the office, for the scientific and non-scientific conversations, and to whom I wish the best on their PhD journey. Thanks to everyone in the NaS group who made me feel very integrated from the start: Lidiia, Matheus and Umberto, and to the colleagues in the Chemical Physics Division with whom I shared many scientific discussions, Thursday pancakes and many lunch breaks that made everything a little easier.

Lund has been a warmer place thanks to all the people who made it special. From my friends from exchange who encouraged me to stay here and whose occasional meetups bring me such joy, to Dominik, Panos and Eftychia for bringing a bit of the Mediterranean here. My corridor housemates who have given me such a great living environment and uncountable memories: the movie nights, the nights out and the small kitchen conversations that made some gray days a little less gray. Rosa, whose friendship goes back to high school and now we are both in Scandinavia pursuing our dreams. It is always a pleasure to cross the bridge and share so many good memories.

My heartfelt appreciation goes to all my friends back home for the love and support they have consistently shown from the distance, for giving me such a warm welcome every time I come back and for believing in me even when I was the most doubtful.

And I could not have done this without my family, who despite having chosen such a different path has always been incredibly supportive and specially my mother, for giving me this education and always being by my side even with the distance.

Contents

List of Abbreviations

- **SOC** : Spin-Orbit Coupling
- **CISS** : Chirality-Induced Spin Selectivity
- **TA** : Transient Absorption
- **RP** : Ruddlesden-Popper
- **LC** : Large Cation
- **HP** : Halide Perovskite
- **MBA** : α-Methylbenzylamine
- **RAC** : Racemic
- **CPL** : Circularly Polarized Light
- **CD** : Circular Dichroism
- **DP** : Dyakonov-Perel
- **EY** : Elliott-Yafet
- **BAP** : Bir-Aronov-Pikus
- **LP** : Linearly Polarized
- **RCP** : Right Circularly Polarized (σ^+)
- **LCP** : Left Circularly Polarized (σ^-)
- **GS** : Ground State
- **ES** : Excited State
- **GSB** : Ground State Bleach
- **ESA** : Excited State Absorption
- **SE** : Stimulated Emission
- **IRF** : Instrument Response Function
- **DMF** : Dimethylformamide

- **ACN** : Acetonitrile
- **CPA** : Chirped Pulse Amplification
- **CCD** : Charge-Coupled Device
- **CP-TA** : Circularly Polarized Transient Absorption

Chapter 1

Introduction

The ability to manipulate the spin degrees of freedom in a solid state is also known as spintronics. This emerging field studies devices that use spin polarized currents for processing and storing information offering new frontiers in optoelectronic devices. When a disequilibrium is created in spin population we have what is called spin polarization. From spintronics both fundamental and more practical questions arise. On the fundamental side one may ask themselves how can this spin polarization be created, how long this disequilibrium on the spin states can last and how can one detect it. Traditionally external magnetic fields have been used to create spin polarization. In 1999 Naaman's group observed that when electrons passed through a chiral organic molecule, the spin orientation depended on the handedness of the chiral molecule with one spin orientation being preferred over the other [30]. This phenomenon now known as chirality-induced spin selectivity (CISS) provided a new way of polarizing spin without the use of magnetic fields [26]. Although highly studied, CISS remains not fully understood and a complete theory is still lacking [12]. Yet ,this phenomenon has been studied in different fields and its applications tested.

Chirality - the property of an object that cannot be superimposed onto its mirror image - is the structural requirement for CISS to occur. Bringing CISS from isolated organic molecules into a solid-state semiconductor requires a material where chirality and strong spin-orbit coupling (SOC) coexist. Metal halide perovskites are well suited for this. They consist of a heavy-metal halide inorganic framework (in this case PbI_6 octahedra) that carries strong SOC from the Pb atom, and a layered structure where organic cations sit between the inorganic substructure [36]. This separation means a chiral organic cation can be introduced without disrupting the optoelectronic properties of the inorganic sublattice. When the organic spacer is chiral, its structural asymmetry is transferred to the PbI_6 net, generating a chiral structure with spin-selective optical properties [22]. The material studied in this work, $(R/S/RAC\text{-}MBA)_2PbI_4$ (MBA = α-methylbenzylamine), belongs to this class of two-dimensional (2D) layered perovskites, where R and S denote the two mirror-image enantiomers and RAC the racemic mixture of both [18].

Circularly polarized light (CPL) carries angular momentum $\pm\hbar$, and through the spin selection rule, preferentially populates one spin state over the other depending if its righ or left polarized, making it a good tool for both generating and assessing the spin polarization of these materials [35].
The amount of time that it takes for the two spin states to equilibrate after light excitation is known as the spin lifetime τ_s. In chiral 2D perovskites it has been measured by using circularly polarized transient absorption (CP-TA) spectroscopy [37, 39], with reported values ranging from tens to hundreds of picoseconds depending on sample composition, measurement conditions, and fitting model. The standard method constructs the spin signal as the intensity difference between co-circular and counter-circular pump-probe configurations [26]. While broadly adopted, it carries two implicit assumptions: it attributes the entire intensity difference to spin relaxation alone, and it assumes that circularly polarized excitation creates a fully pure-spin population. Given that a complete theory of CISS is yet to be established, these assumptions may not hold. In this thesis we address two questions: **(i)** how does the CISS effect manifest in the spin dynamics of (R/S/RAC-MBA)$_2$PbI$_4$, and **(ii)** can a kinetic rate equation model that explicitly separates the different decay pathways after excitation provide a more complete picture of spin dynamics than the conventional helicity-difference method?

Here, we use transient absorption spectroscopy with circularly polarized pump ($\lambda = 480$ nm) and broadband probe pulses at four pump-probe helicity combinations to study the spin-dependent carrier dynamics of R-, S-, and RAC-MBA$_2$PbI$_4$ thin films. Spin lifetimes are extracted by both the helicity-difference method and a proposed kinetic model. The two approaches are compared and connected to assess the accuracy and completeness of each.

Thesis Outline

Framework of this thesis is set to facilitate the understanding of the research. In Chapter 2 we start by setting the theoretical concepts needed to understand the results. An overview on the sample structure is given, followed by an explanation of chirality and the chiral induced spin selectivity effect. The concepts of polarization of light and the main technique used, transient absorption spectroscopy, are also covered. Chapter 3 describes the synthetic methods use to prepare the samples and the characterization techniques used as well as a walkthrough of the transient absorption setup. On Chapter 4 the results are presented and discussed. The absorption spectra and circular dichroism spectra are presented and the spin lifetimes reported by the two methods and its results compared.

Chapter 2

Theoretical Background

The following chapter provides the essential theoretical concepts for understanding this thesis. We begin by introducing the material under study: metal halide perovskites. We then discuss the concept of chirality, given that the chiral organic ligands are fundamental to the spin-selective optical properties of these materials and give a word on spin orbit coupling (SOC) and its influence on the optical properties. This is followed by an introduction to the CISS phenomenon. Finally, we introduce the concept of polarization of light and provide an overview of transient absorption (TA) spectroscopy, the primary experimental technique used in this work.

2.1 Metal Halide Perovskites

Perovskites were first discovered by the German mineralogist Gustav Rose in 1839. In 1926, Victor Goldschmidt proposed their crystal structure and introduced the Goldschmidt tolerance factor as a criterion for predicting structural stability.
The crystal structure of a perovskite is shown in Figure 2.1. In the classic ABX_3 perovskite structure, A is a monovalent cation, B is a divalent metal cation, and X is a halide anion. In metal halide perovskites, the B-site is occupied by a heavy metal such as lead (Pb^{2+}) and the X-site by a halide (I^-, Br^-, or Cl^-), forming corner-sharing BX_6 octahedra that constitute the inorganic framework. The optical and electronic properties of the material are primarily determined by this inorganic sublattice, while the A-site cation modulates the lattice geometry and symmetry through hydrogen bonding and steric interactions with the octahedra[33].

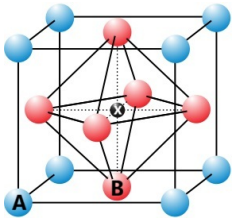

Figure 2.1: Crystalline structure of the classic perovskite where A is a monovalent cation, B is a divalent cation and X is an halide anion. Adapted from [38].

When the A-site cation is replaced by a large cation (LC), the three-dimensional perovskite structure is no longer stable. Instead, the material adopts a layered two-dimensional (2D) Ruddlesden-Popper (RP) structure of general formula $(LC)_2A_{n-1}B_nX_{3n+1}$, where n is the number of inorganic octahedral layers and LC is the organic spacer[24]. This RPs perovskites are good candidates for overcoming some of the stability issues that halide perovskites (HP) present because of the hydrophobic character of the LC and the higher formation enthalpies that make the lattice more resistant, however the higher complexity of the RP structure also presents some stability issues and a new set of engineering possibilities for finding good candidates for solar cells and spintronic devices [31].
In Figure 2.3 the RP structure for n=1 is shown where n is the number of HP layers in between the LC. The optoelectronic properties can be modified by varying the n value, where the exciton binding energy reduces as n is increased [6].

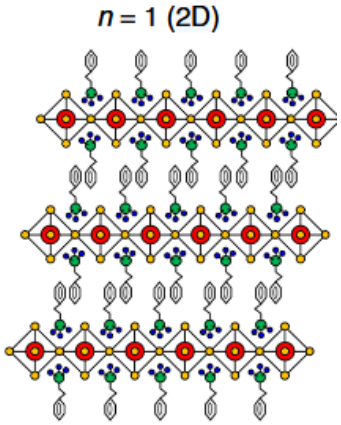

Figure 2.2: Schematic of the RP structure with n being number of HP layers sandwiched between the LC. Credit for Righetto et al. [31].

For $n = 1$, the structure consists of a single inorganic PbX_6 octahedral monolayer sandwiched between bilayers of organic cations. The organic layers act as both quantum and dielectric barriers, confining the electronic wavefunctions to the inorganic sheets and dramatically modifying the optical response relative to their 3D counterparts.
The quantum confinement and the large dielectric contrast between the inorganic and organic layers makes the excitons[1] (electron and hole paired) in the molecule to have high binding energies (between 470-150 meV from n=1 to n=4), larger than room temperature fluctuations (k_BT) [6]. As a result, the optical response of 2D RP perovskites is dominated by excitonic transitions even at ambient conditions.

[1]Recall that an exciton is a quasiparticle formed by an electron and a hole bounded by its mutual Coulomb interaction. After light excitation the electron gets promoted to the conduction band of the material while the hole stays in the valence band.

In this work, the LC is α-methylbenzylamine (MBA^+), a chiral molecule that has two enantiomeric forms: (R)(+)-MBA and (S)(−)MBA. When incorporated at the LC-site cation, the chiral MBA molecule transfers its structural asymmetry to the PbI_6 inorganic framework inducing a chiral distortion of the octahedral structure. The asymmetric hydrogen-bonding interaction between the LC and the inorganic substructure plays a role in the chiroptical activity of the perovskite [22]. This results in a chiral 2D perovskite: $(R/S/RAC\text{-}MBA)_2PbI_4$ where the handedness of the organic cation is imprinted onto the electronic structure of the inorganic layer, enabling spin-selective optical excitation [18].
Pb also plays an important role here, the heavy metal introduces strong SOC that, combined with the broken inversion symmetry inherent to the layered structure, produces Rashba-Dresselhaus spin splitting of the electronic bands, a feature of central importance for spin-dependent phenomena [37].

2.2 Chirality

A molecule or object is defined as chiral if it cannot be superimposed onto its mirror image. The two non-superimposable mirror image forms are called enantiomers, conventionally labeled (R) and (S) according to the Cahn-Ingold-Prelog priority rules, or (+) and (−) according to the direction in which they rotate plane-polarized light. Its worth noting that (+) and (−) depend on the convention.
Chirality arises from the absence of improper symmetry elements (mirror planes, inversion centers or improper rotational axes) in the molecular or crystal structure.

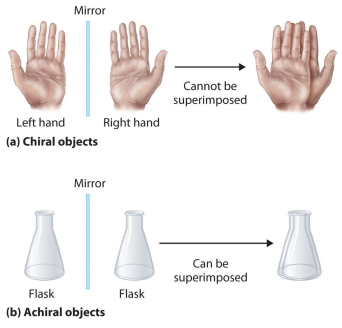

Figure 2.3: Example of a chiral and achiral object. Image adapted from [20].

While the two enantiomers of a chiral molecule share identical scalar physical properties (melting point, refractive index, bond lengths) they differ in their interaction with circularly polarized light (CPL), giving rise to chiroptical phenomena. On the other hand, an achiral molecule will not distinguish between right or left

CPL giving null chiroptical activity.
The most fundamental chiroptical measurement is circular dichroism (CD), defined as the differential absorption of left- (σ^-) and right- (σ^+) circularly polarized light [40]:

$$\Delta A_{CD}(\lambda) = A_R(\lambda) - A_L(\lambda) = [\varepsilon_R(\lambda) - \varepsilon_L(\lambda)]\, lC = \Delta\varepsilon(\lambda)\, lC, \tag{2.1}$$

where A_R and A_L are the absorbances of right- and left-circularly polarized light, ε_R and ε_L are their respective molar absorptivities, l is the path length, and C is the concentration. The CD signal is typically small — on the order of 10^{-3}–10^{-4} of the total absorption coefficient — and is commonly expressed in millidegrees (mdeg) of ellipticity [40]. CD is only observed at wavelengths where absorption occurs: the signal arises from the interaction between different transition dipoles during the absorption process, which is dependent on their relative orientation in space.

A nonzero CD signal is direct spectroscopic evidence of broken mirror symmetry [40]. For a pair of enantiomers, the CD spectra are equal in magnitude and opposite in sign, as the two mirror-image structures interact with opposite helicities[2] of light with the same strength but opposite sign. Equation 2.2 shows how the CD spectra is calculated from the CD absorption measurements.

$$CD = \Delta A \left(\frac{ln10}{4}\right)\left(\frac{180000}{\pi}\right) \tag{2.2}$$

CD spectra is a great tool for identifying isomers of a molecule, given that their physical properties such as molecular weight or melting point would be the same.
Having introduced the concept of chirality we can move on to explaining a phenomena that arises from this, the chiral induced spin selectivity, central on our work.

2.3 The CISS Effect

Chirality-induced spin selectivity (CISS) is the phenomenon by which the movement of charges through a chiral medium results in a spin-polarized current, without the need for magnetic components and operating at room temperature [36]. In layman terms it can be understood as if an achiral molecule, just by proximity to a chiral molecule will get impregnated from its chirality and show chiral optical behavior. The effect was first observed in 1999 by Ray, Naaman and Waldeck [30], who reported preferential scattering of spin-polarized electrons passing through oriented chiral molecules, a result incompatible with the expected magnitude of SOC from

[2]Chirality refers to the general concept but helicity can only be related to the angular momentum, parictular of light[8].

light organic atoms alone. Since then, CISS has been confirmed in a wide range of chiral media and has evolved into an umbrella term for phenomena in which molecular handedness gives significant spin selectivity to electron processes [12].
The natural mechanism to call for CISS is spin-orbit coupling (SOC), given the connection between chirality and spin. A complete quantitative theory remains yet to be found and the microscopic origins of CISS are still not fully understood [12].
From theoretical work it has established that a chiral molecules break parity symmetry but retain time-reversal symmetry. When a charge flows through a chiral molecule, time-reversal symmetry is broken and a magnetic field is generated along the direction of charge motion. As an electron moves along the chiral potential of the molecule, it experiences a Rashba-type [3] SOC term that couples its linear momentum to its spin. In Figure 2.4 this energy splitting is described. A freely propagating electron has four states associated with its motion: $|+,+\rangle$, $|-,-\rangle$, $|+,-\rangle$, and $|-,+\rangle$, where the first index denotes the direction of motion and the second the spin orientation [27]. The SOC stabilizes one state and destabilizes its counterpart by the same energy H_{SO}, so the energy difference between spin levels is $2H_{SO}$. Notice how the state $|+,+\rangle$ is degenerate with $|-,-\rangle$. Because the chiral molecule will prefer one spin orientation with one direction and the exact opposite.[27].

[3]Rashba splitting is the energy difference between spin states in a system due to inversion symmetry breaking

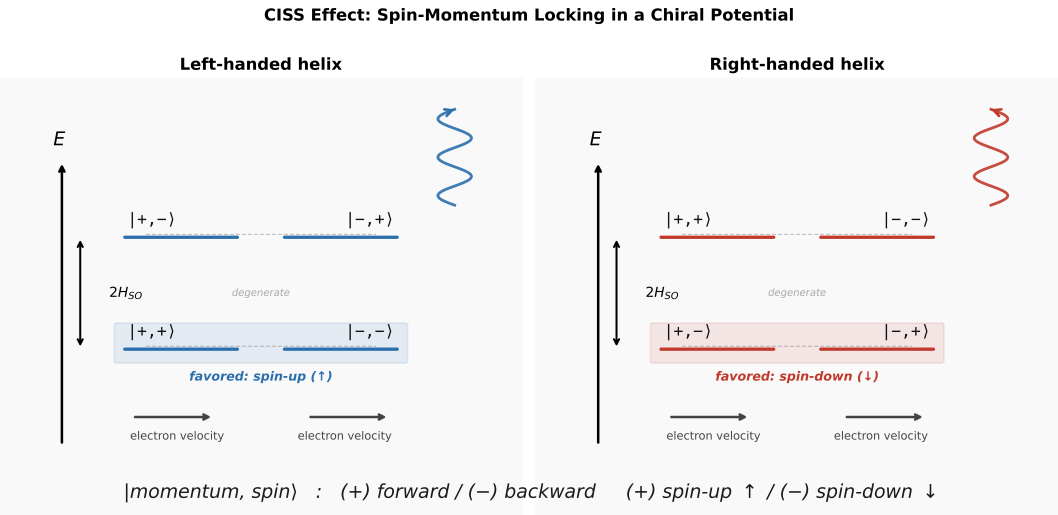

Figure 2.4: Energy scheme of the momentum-spin states $|\text{momentum, spin}\rangle$ for an electron moving within a chiral potential for a left-handed and right-handed helix. The spin-orbit coupling splits the states by $2H_{SO}$, stabilizing one spin channel and destabilizing the other. The favored spin orientation flips with the handedness of the helix, illustrating the spin-filtering action of the CISS effect: one helicity of motion is preferred for one spin direction. The notation $(+)$ and $(-)$ refer to forward and backward electron motion respectively, and spin-up $(\uparrow)$ and spin-down $(\downarrow)$ respectively. Adapted from Naaman and Waldeck [27].

Once spin-polarized carriers are created, their spin orientation decays toward equilibrium through spin relaxation. Spin transport differs fundamentally from charge transport in that spin is not a conserved quantity in solids, due to spin-orbit and hyperfine coupling [35]. Three main mechanisms govern spin relaxation in semiconductors:

The **Dyakonov-Perel (DP)** mechanism dominates in systems with broken inversion symmetry [35]. The k-dependent spin splitting acts as an effective internal magnetic field whose direction and magnitude depend on the crystal momentum. At each momentum scattering event, the direction of this effective field changes, causing the spin to precess in a different direction at each step. The spin relaxation time τ_{DP} is therefore inversely proportional to the momentum scattering time: more scattering means more frequent changes in precession axis and faster spin dephasing [35, 10].

The **Elliott-Yafet (EY)** mechanism operates in systems with inversion symmetry and arises from spin-flip scattering at phonons or impurities [35]. Because spin-orbit coupling mixes spin-up and spin-down components into every Bloch state

[4], each momentum scattering event carries a finite probability of also flipping the spin. In contrast to DP, the EY spin relaxation time is proportional to momentum scattering: more scattering events mean more opportunities for spin flip. Its important for small gap semiconductors that present a large SOC.[35, 11].

The **Bir-Aronov-Pikus (BAP)** mechanism is specific to conductor electrons in p-doped semiconductors where both electrons and holes are present [35]. It arises from the electron-hole exchange interaction: when a spin-polarized electron interacts with a hole, the exchange coupling can flip the electron spin. It dominates heavy doped samples at low temperatures [35].
In 2D RP perovskites, all three mechanisms may contribute and they can be distinguished by their density and temperature dependence.

2.4 Polarization of Light

The polarization state of a monochromatic electromagnetic wave describes the trajectory traced by the electric field vector E in the plane perpendicular to propagation. For a wave propagating along $\hat{z}$, the two orthogonal field components are:

$$\mathbf{E}(t) = \begin{pmatrix} E_x \\ E_y \end{pmatrix} = \begin{pmatrix} A_x e^{i\delta_x} \\ A_y e^{i\delta_y} \end{pmatrix} e^{i(kz-\omega t)}, \tag{2.3}$$

where A_x, A_y are the real amplitudes and δ_x, δ_y are the phases of each component. The polarization state is fully described by the complex Jones vector[32]:

$$\mathbf{J} = \begin{pmatrix} A_x e^{i\delta_x} \\ A_y e^{i\delta_y} \end{pmatrix}. \tag{2.4}$$

On this thesis, three polarizations are used: linear polarization (LP), right circular polarization (RCP) and left circular polarization (LCP):

- **LP**: A_x, A_y arbitrary, $\Delta\delta = \delta_y - \delta_x = 0$ or π.
- **RCP** (σ^+): $A_x = A_y$, $\Delta\delta = +\pi/2$.
- **LCP** (σ^-): $A_x = A_y$, $\Delta\delta = -\pi/2$.

Any deviation from $A_x = A_y$ or $\Delta\delta \neq \frac{\pm\pi}{2}$ produces elliptically polarized light. The degree of circular polarization is quantified by the Stokes parameter:

$$\rho_c = \frac{S_3}{S_0} = \frac{2A_x A_y \sin(\Delta\delta)}{A_x^2 + A_y^2}, \tag{2.5}$$

[4]Bloch states are the fundamental quantum wavefunctions used to describe the electrons moving in a periodic potential such as a crystalline structure

where $S_0 = A_x^2 + A_y^2$ is the total intensity and $S_3 = I_{\sigma^+} - I_{\sigma^-}$. For perfect circular polarization $\rho_c = \pm 1$; for linear polarization $\rho_c = 0$. In a real optical setup, waveplates and other optical devices introduce retardation errors ϵ that shift $\Delta\delta = \pi/2 + \epsilon$, accumulating along beam path, reducing the degree of circular polarization below unity.

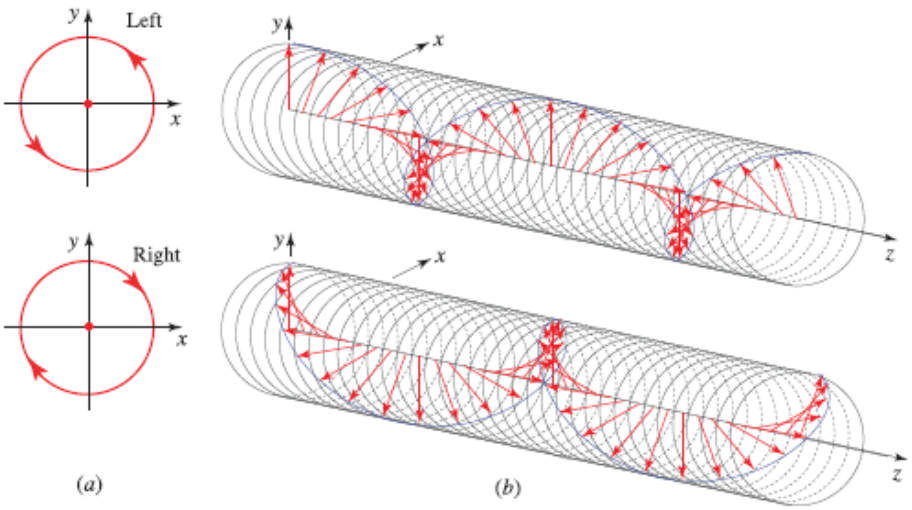

Figure 2.5: Motion of the endpoints of the electric-field vectors for left and right circularly polarized plane waves, (a) Time course at a fixed position z.(b) Trajectories of the endpoints. Image from Bahaa E. A. Saleh, Malvin Carl Teich, Fundamentals of Photonics [32].

Circularly polarized photons carries angular momentum $\pm\hbar$ along the propagation axis. Conservation of angular momentum in optical absorption gives the selection rule $\Delta m_J = \pm 1$ for $\sigma^{\pm}$ light, making circularly polarized excitation the primary tool for creating spin-polarized carrier populations in semiconductors.

2.5 Transient Absorption Spectroscopy

Transient absorption (TA) is a spectroscopy technique used to study the photodynamics of a species under light excitation. This technique, also known as pump-probe, uses two pulses. The first pulse, the pump, has a fixed wavelength selected to excite the transition of interest, typically matching the energy difference between the ground state (GS) and the excited state (ES). The second pulse, the probe, passes through the sample at a controlled delay time Δt and covers a broad range of wavelengths (typically 350 - 1300 nm), tracking the changes in absorption induced by the pump light. A scheme of the two-pulse configuration is shown in Figure 2.6.

By varying Δt, one obtains the evolution of the absorption spectrum as a function of time after excitation. The TA signal is defined as the differential absorbance:

$$\Delta A = A_{\text{pump on}} - A_{\text{pump off}}. \tag{2.6}$$

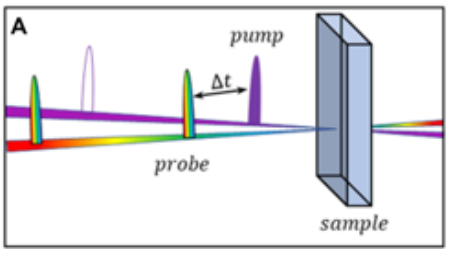

Figure 2.6: Scheme of the pump probe pulses configuration on TA. Adapted from Jia et al. [19]

A negative ΔA indicates reduced absorption after excitation, while a positive ΔA indicates increased absorption. The measured TA spectrum is the superposition of three main contributions, illustrated in Figure2.7. The ground state bleach (GSB) arises because pump excitation depletes the ground state population, reducing the absorbed light at the GS to ES transition energy and producing a negative ΔA. The excited state absorption (ESA) occurs when probe photons drive transitions from the populated ES to higher excited states, producing a positive ΔA. Stimulated emission (SE) occurs in systems where the probe photons stimulate radiative decay from the ES back to the GS, increasing the detected probe intensity and therefore producing a negative ΔA.[19].

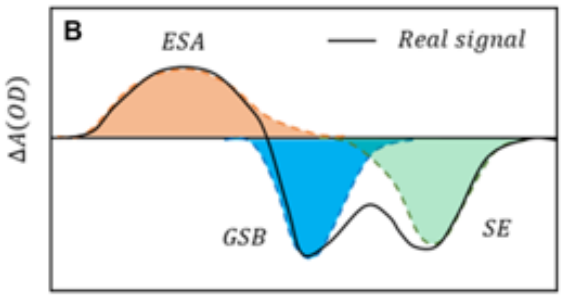

Figure 2.7: Scheme of a usual TA spectra with the main peaks generally observed. Adapted from Jia et al. [19]

Chapter 3

Methods

The next section provides with a detailed information about the synthesis and characterization of the samples reported in this project. This section provides with information on the synthesis and thin film preparation as well as the characterization techniques used with a description of the TA measurements done in Millenia Lab in the Division of Chemical Physics.

Acknowledgments: The experiments reported in this Master Thesis by Jan Planelles were performed under the supervision of Dr. Prasenjit Mandal Dr. Sankaran Ramesh with Prof. Dmitry Baranov as Principal Investigator (PI) and scientific advise of Prof. Tönu Pullerits. SR, PM, DB, TP and JP conceptualized the experiments. SR, PM and JP modified the Transient Absorption (TA) setup. PM synthesized and fabricated the chiral $(R/S/RAC-MBA)_2PbI_4$ perovskite crystals and PM and JP prepared the thin films. JP conducted the data analysis.
The work was possible thanks to the funding from the European Innovation Council (EIC) Pathfinder Challenges program under Grant No. 101162112 (RADIANT) and the Swedish Research Council (2024-04967).

3.1 Synthesis of $(R/S/RAC - MBA)_2PbI_4$

3.1.1 Synthesis of $(R/S - MBA)_2PbI_4$

Synthesis of $(R/S - MBA)_2PbI_4$ was conducted following the protocol reported previously by Makhija et al. [23]. Lead(II) oxide (PbO) (0.558 g, 2.5 mmol) was dissolved in 10 mL of hydroiodic acid (HI) and 2 mL of phosphinic acid aqueous solution in a 20 mL glass vial. The mixture was heated at 70 °C and stirred magnetically at 400 rpm. After solution becomes clear, the enantiomer (R)-(+)-(σ)-methylbenzylamine (5 mmol, 637 μL) was added, resulting in the formation of orange-colored crystals. The mixture was then reheated under constant stirring to yield homogeneous yellow solution, indicating that all crystals had dissolved. The solution then let to cool at room temperature. The synthesized mixture was left undisturbed overnight to complete the crystallization process. After crystallization, the crystals were filtered, washed with diethyl ether, and subsequently dried under vacuum. Then stored in a glove box for further use [5].

3.1.2 Synthesis of $(RAC - MBA)_2PbI_4$

The synthesis of (rac-MBA)$_2$PbI$_4$ was carried out following a modified version of the procedure reported by Ahn *et al.* [1]. PbO (200 mg, 0.896 mmol) was dissolved in 6 mL of 57% HI solution in a 20 mL glass vial under continuous magnetic stirring. Subsequently, 200 μL (1.57 mmol) of racemic MBA, consisting of an equimolar mixture of the (R)- and (S)-enantiomers, was added to the solution, resulting in the immediate formation of a precipitate. The reaction mixture was then heated to 100 °C in an oil bath until the precipitate fully dissolved. After complete dissolution, the solution was allowed to cool naturally to room temperature under ambient conditions, leading to the formation of orange needle-shaped crystals. The obtained crystals were isolated by vacuum filtration and washed several times with toluene. Finally, the product was dried under vacuum in a desiccator for a minimum of two days and subsequently stored in a nitrogen-filled glovebox prior to further use.

3.1.3 Thin Film Preparation

Before film deposition, glass substrates (1×1 cm^2) were cleaned with isopropyl alcohol and dried using compressed air to eliminate any residual contaminants. Thin films of (R-MBA)$_2$PbI$_4$ or (rac-MBA)$_2$PbI$_4$ were prepared by dissolving 4 mg of the synthesized chiral crystals in a solvent mixture containing 10 μL of dimethylformamide (DMF) and 250 μL of acetonitrile (ACN). The resulting solution was homogenized using a vortex mixer.

Prior to deposition, both the precursor solution and the glass substrates were heated to 70 °C. Subsequently, 40 μL of the heated solution was deposited onto the substrate either by drop-casting or by spin coating. For spin coating, the substrates were rotated at 1000 rpm for 10 s followed by 3000 rpm for 30 s. After deposition, the films were annealed on a hot plate at 60 °C for 5 min.

To improve environmental stability, both drop-cast and spin-coated films were encapsulated with a polyester layer applied via spin coating. This protective coating minimized exposure to moisture and other contaminants. The completed films were subsequently stored in a nitrogen-filled glove box. Encapsulated spin-coated films with polystyrene protection were further utilized for steady-state absorption spectroscopy, circular dichroism, and transient absorption measurements.
A total of four thin films were prepared for each sample to ensure reproducibility and consistency in film quality. Variations during the spin-coating process can lead to differences in film deposition, resulting in some samples being more concentrated or more homogeneous than others.

3.2 Characterization of $(R/S/RAC - MBA)_2PbI_4$

The thin films on glass substrates were used for Steady State Absorption spectroscopy, circular dichroism (CD) spectroscopy and transient absorption (TA) measurements. Steady State Absorption spectra and CD spectra were measured using OLIS DSM 245 CD/CPL Spectrophotometer equipped with a 150 W Xenon lamp. Absorption spectra was used to ensure that the right materials were synthesized and CD spectra is used to check the chirality transfer of MBA_2 to the perovskite and that racemic sample does not have chiral optical response. The TA measurements were done in the Millenia Lab using the Solstice setup during week 40,44 and 48 of 2025 and week 8 of 2026.

3.2.1 Transient Absorption Spectra

In Figure 3.3 a schematic of the TA set up is shown. Let's walk through it.
The laser system is called Solstice (See Figure 3.1), this system consists of a seed laser pulse (called MaiTai), a chirped pulse amplification (CPA) system where Regen is the amplifying cavity and a pumping laser (Ascend) that pumps the crystal in the Regen cavity.
The MaiTai generates the seed pulse, this pulse is short and weak, the short pulse is obtained by mode-locking, an optical technique to obtain very short pulses (way shorter than the one we will obtain at the end). This short pulse is stretched and

then sent to the Regen cavity. In the Regen cavity is met with the Ascend laser, this laser will amplify the laser pulse at the Regen cavity. In this cavity the power is amplified and then sent to a compressor to optimize stability and maximum power output. The final pulse has 796 nm, with an ideal power of 8 Watts, a repetition rate of 4 kHz and a pulse of roughly 60 fs. In Figure 3.3 this Solstice system is summarize all in the Amplifier box. The pulse that comes out is then split into two: half will be send for the pump and half for the probe. Then both the pump and probe go through the TOPAS (optical parameter amplifier). On the pump TOPAS, with the use of non-linear optical processes, we can convert the 800 nm wavelength in the desired wavelength. In our case, for creating 480 nm, 1200 nm and 800 nm are mixed. These interactions depend on the polarization of the beam, which depend on the rotation of the mixing crystals. On the TOPAS, Crystals and Delays can be changed to optimized the wavelength and amplitude of the pump. After the TOPAS, two filters are used to take away other wavelengths residue there might be. Two mirrors and two pinholes are used to align the beam, recall that with the first mirror we align in the first pinhole and the second mirror for the second pinhole. The beam then goes through the chopper which takes out half the pulses (has a repetition rate of 2 kHz) because in TA we observe the difference in absorption when pump is on and off. Then it goes through the Berek compensator that modifies the polarization of the collimated beam. The probe is set to haver vertical polarization so we set the pump to have horizontal polarization to reduce the scattering of the pump when measuring. After the Berek compensator, for the case of circular polarized TA a quarter waveplate (Thorlabs AQWP05M-600) is added to change the linearly polarized light into circularly polarized light.

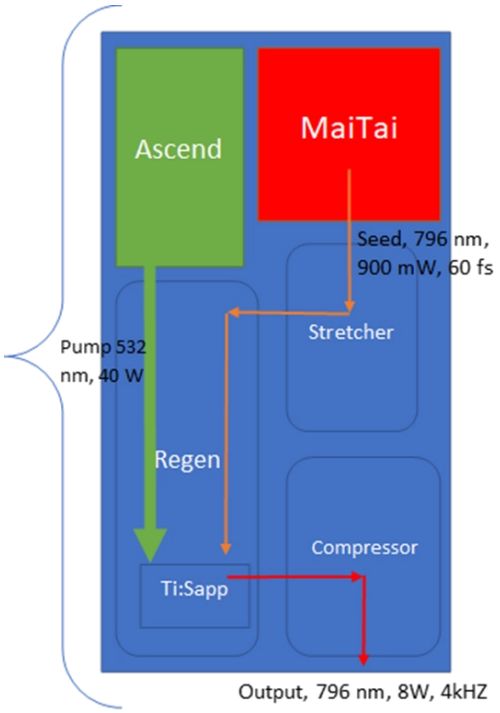

Figure 3.1: Scheme of the laser system Solstice composed of a seed pulse (MaiTai),an Ascend cavity that pumps the laser and Regen cavity that amplifies the pulse. It generates pulses of 796 nm with a power of 8 W and a repetition rate of 4 kHz with a pulse duration of approximately 60 fs.

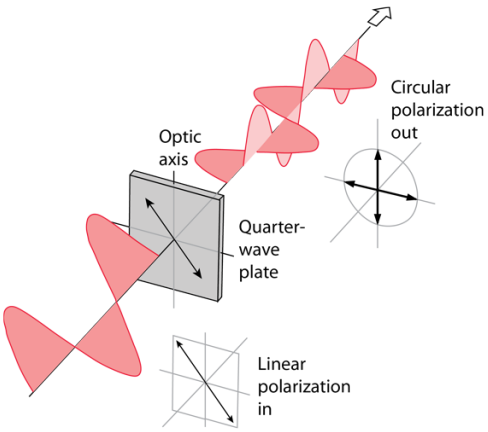

Figure 3.2: Production of CPL from LP light [28]

Also, a waveplate does not attenuate the intensity of the field, it changes the phase. The beam then goes through two filter wheels that will be used to change the power intensity of the beam. Different lenses can be used also to get the best beam profile (ideally Gaussian like). The beam profile is seen by using a CCD camera, the pump and probe diameters are also noted and the beams overlapped. The pump should be at least 3 times bigger than the probe to make sure that all the probed area has been excited. The probe white light is generated with a calcium fluoride (CaF_2) crystal. Before going through the sample the probe beam is divided into reference and sample. The reference beam is sent straight to the photodiode array, the sample probe after going through the sample also sent to another photodiode array collecting all the data points.

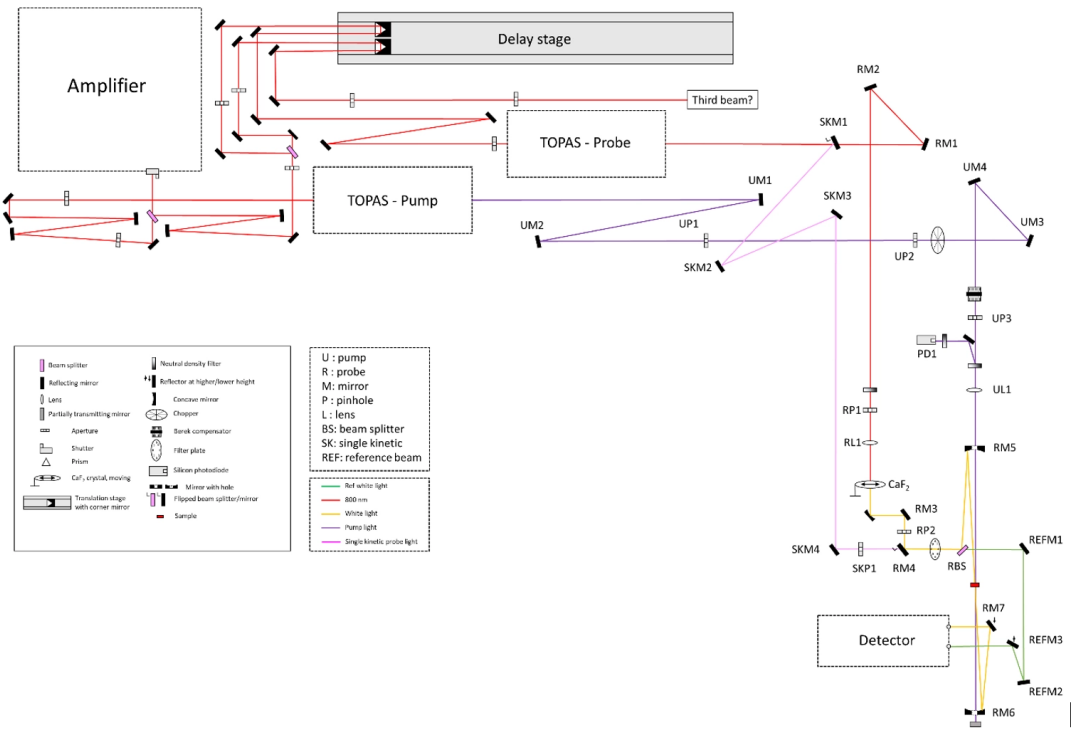

Figure 3.3: Scheme of Transient Absorption set up in Millenia Lab

In order to know the fluence (uJ/cm^2) the beam size needs to be calculated. With CCD camera the beam diameter (d) is known and with the help of a powermeter the fluence can be easily calculated:

$$Fluence(\frac{uJ}{cm^2}) = \frac{P(uW)}{2000\pi(\frac{d(cm)}{2})^2} \tag{3.1}$$

TA Spectra was collected for the different polarization configurations and in the linear polarization setting for a range of fluence between 3 and 100 uJ/cm^2 although at the end only circularly polarized sets were used in this study. For the different polarizations configurations only one fluence was used: 8 uJ/cm^2. Labeling of the data sets will have pump - probe configuration with polarization, either $\sigma+$ or $\sigma-$, referring to right or left circularly polarized light. All the data has been analyzed with custom-made Python notebooks and the help of Generative-A.I. For all data files, scattering and chirp correction has been done as a first step of the analysis. Then Lorentzian functions (Equation 3.2) are used to fitting and later the kinetic analysis is done. For most of the kinetic analysis done in this project one wavelength of interest is selected, meaning that we study the change of TA signal for a chosen wavelength, a more complete but also challenging analysis would be global analysis,

meaning fitting and studying the kinetics for the whole spectra.

$$y = \frac{Ag^2}{(x - x_0)^2 + g^2} \tag{3.2}$$

Table 3.1: Time Points configuration used in the measurements. First column refers to from which time point, second column until which time and the Steps column every how much time to measure. Notice how at longer times the steps are set logarithmic since at longer times of the delay the noise increases and we are also not interested in such longer time scales.

From	**To**	**Steps**
- 11	- 1	2 ps
- 1	1	0.1 ps
1	3	0.2 ps
3	15	1 ps
40	9000	100 steps (log)

Chapter 4

Results and Discussion

The results section starts with analysis of the steady state absorption spectra and circular dichroism of $R, S, RAC - MBA_2PbI_4$ followed by an analysis and kinetic study of the TA spectra for different pump probe polarizations. For the TA analysis the spectras are fitted with Lorentzian functions and then the spin lifetimes obtained by two methods: first by intensity difference of different probe polarizations, as done usually in the literature, and by a new proposed kinetic model.

4.1 Absorption Spectra

The absorption spectra (Figure 4.1) was recorded for the R,S isomers and the racemic sample. The peak found at 2.49 eV (500 nm) corresponds to the excitonic band. After excitation, an electron bounded to a hole is excited to the conducting band and sits just below it, the electron and hole are bounded by coloumbic interaction. At higher energies (3.2 eV) the interband is found, from free electrons going from the valence band to the conducting band. Notice how the excitonic peak is stronger for the R isomer than S and racemic.

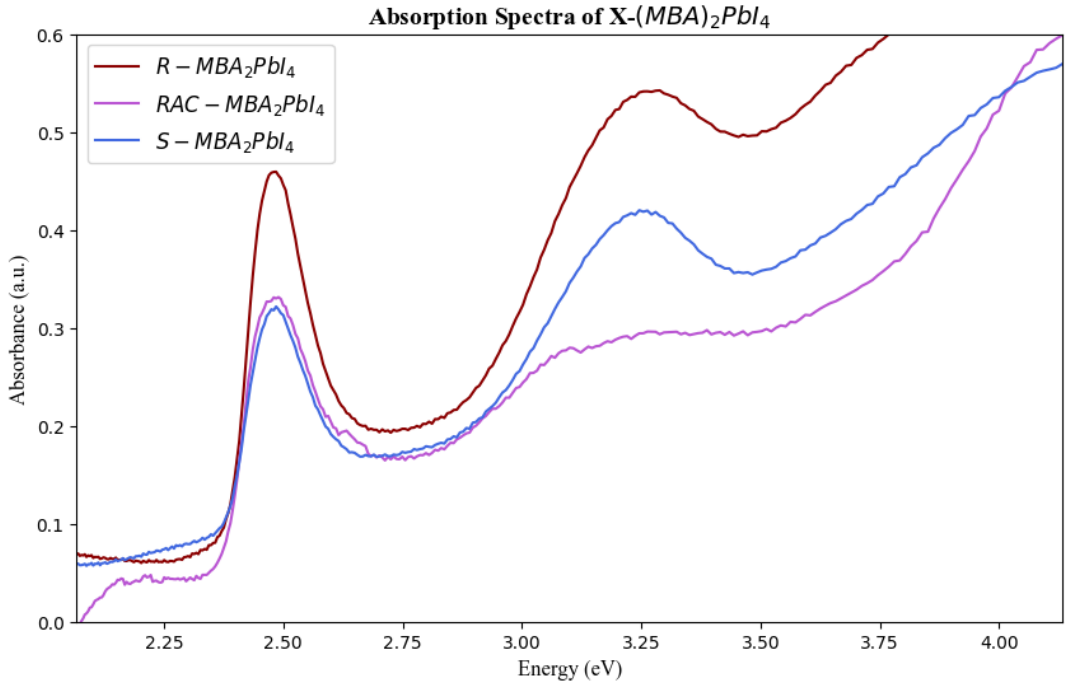

Figure 4.1: Absorption Spectra Measured for the isomers and the racemic sample.

Although the concentration is set to be the same for all the isomers, when preparing the thin film the exact concentration is not known. Same difference has been observed in literature [37] therefore it could be due the crystalline order of the R isomer giving a higher oscillator strength and hence more absorption. The racemic mixture, since its a mixture of R and S presents higher disorder and therefore it will have a lower oscillator strength giving less absorption.
Measuring the steady state absorption spectra serves as a blue print for the following pump-probe experiments: the wavelength of the pump can be selected so its sits right above the excitonic peak (the same wavelength is not desired since the scattering of the pump would blind any features from that set wavelength).

4.2 Circular Dichroism

In Figure 4.2 the Circular Dichroism (CD) spectra is shown. CD spectra measures the absorption difference when left and right circularly polarized are used. The non zero signal in CD means that there is an asymmetry in the molecule [3]. For a pair of enantiomers like R,S, their CD spectra will be of opposite sign.
Recall that PbI_4 is an achiral perovskite, and we have added a chiral ligand to see if there is some chirality transferred. Notice in Figure 4.2, the peak at 2.5 eV for the R,S enantiomers due to the excitonic band, consistent with previously reported values [37] [21], exposing that there has been chirality transfer to the exciton. From literature we know that this peak does not belong to the ligand transition since the

$\pi \rightarrow \pi*$ transition of MBA^+ is at 270 nm (4.5 eV) [14]. The excitonic peak has a bisegnate shape due to the Cotton effect (close to the absorption wavelength the CD signal changes drastically of sign crossing zero at the absorption).

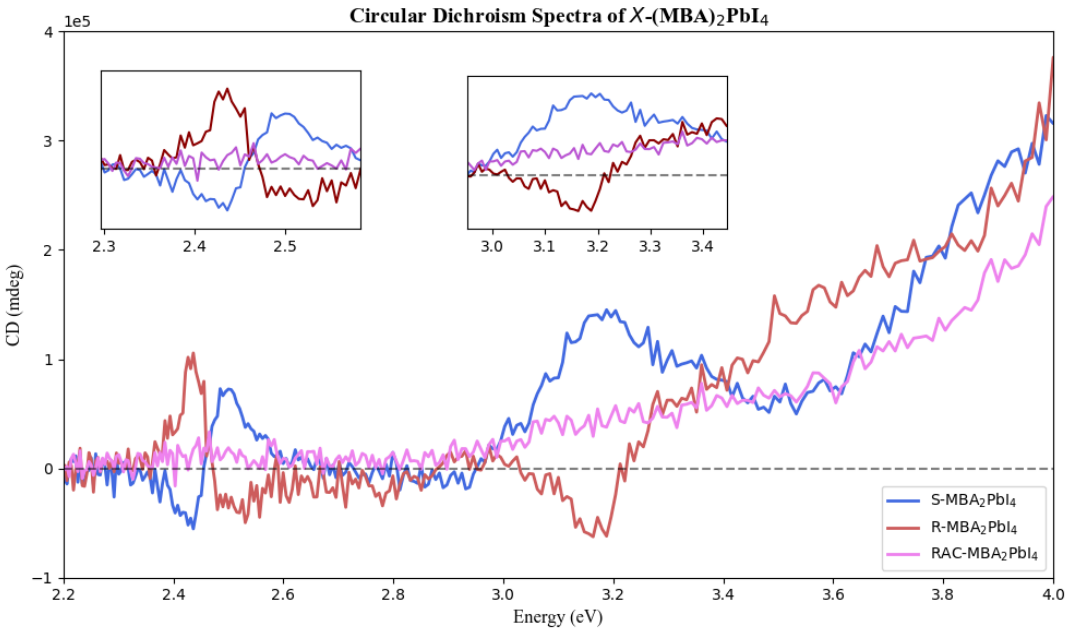

Figure 4.2: Circular Dichroism spectra of $X - MBA_2PbI_4$

At the interband, 3.2 eV, a nonzero CD signal is also observed, which means that chirality has also been transferred to the crystalline structure. The Racemic sample does not present CD signal at the excitonic peak due to lack of total chirality when both enantiomers are mixed in equal quantities. Still, a small positive peak is observed for RAC. This is due that although the sample is racemic there can be some local domains where a certain isomer is more prominent or also that that particular thin film or the spot where pumped it has a preferred structure. The broad band starting at 3 eV for the racemic mixture could be to linear dichroism and crystal orientation and not related to chirality presence specifically.

4.3 Transient Absorption Spectra Analysis

Figure 4.3 shows the TA spectra of one of the measurements. Scattering and chirp correction is employed at any probed time to obtain the more accurate spectra.

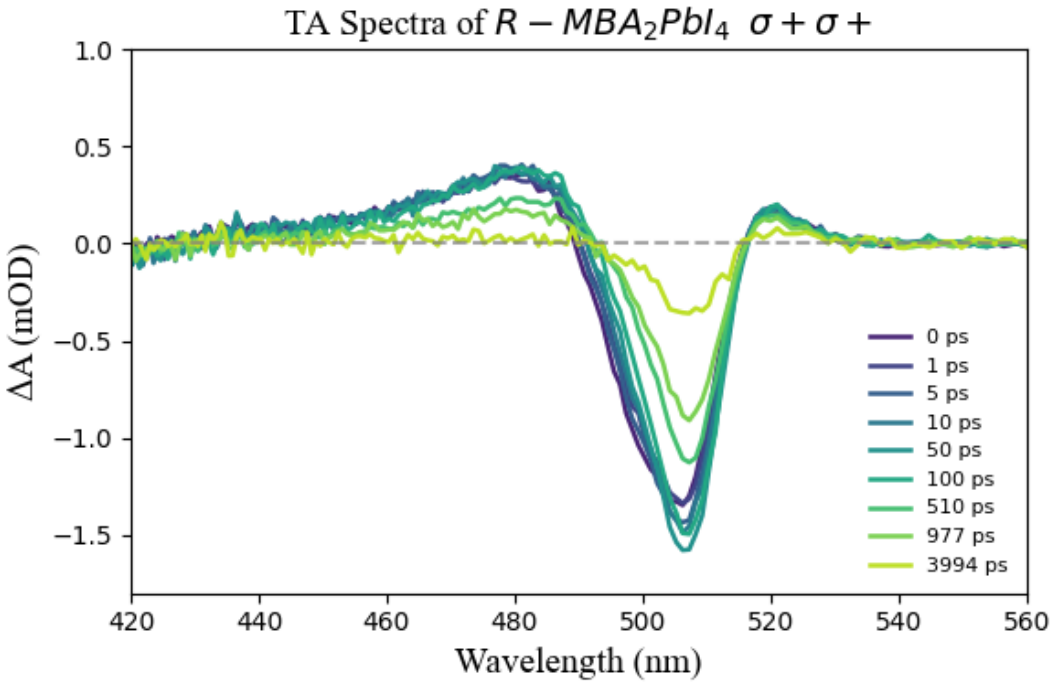

Figure 4.3: TA Spectra at different time delays for $R - MBA_2PbI_4$ with σ^+pump and σ^+probe

Observing the TA spectra for the different polarizations used it can be seen easily the difference of absorption at the peaks and the different decays rates: the photophysics are affected by the polarization of light used. Lorentzian functions were used to fit the peaks (See Figure 4.4). Lorentzian functions were used because the exciton can be understood as a lorentzian oscillator [16](a bound charged particle responding to an electromagnetic field) . The imaginary part of the Lorentz oscillator gives the absorption line shape, frequencies close to the excitonic resonance will behave purely imaginary and since we pump very close to resonance (See Section 4.1) we see the absorption change and hence the use of Lorentzian functions [2].
The GSB shows a negative peak since the sample has absorbed energy of the pump and the electrons have moved to the excited state, therefore there is a decrease in population and less absorption of light. The ESA peaks comes from photo-induced absorption when the energy of the probe light satisfies a transition from the excited state to a higher excited state [19] In an ideal setting, the total area of the GSB should equal that of the newly formed excited states (ESA1 + ESA2), but in reality this is not observed: a discrepancy of approximately 10% is seen. This could be due to stimulated emission hidden within the GSB peak, residual error after scattering and chirp correction (which is a numerical process), and the fact that although the Lorentzian model captures the peaks with precision, the underlying physics may require a more complex line shape model. In the lower right corner of Figure 4.4 the

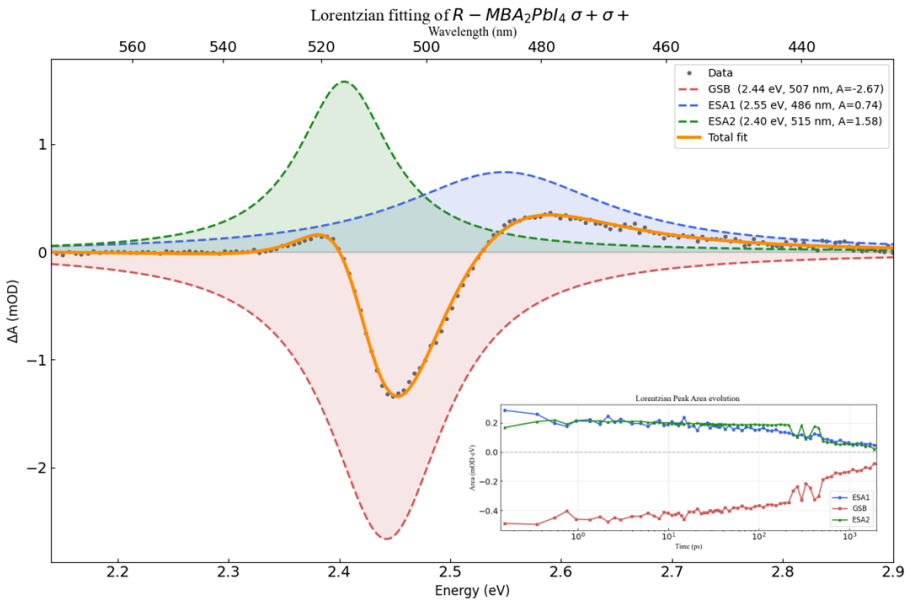

Figure 4.4: TA Spectra at 1ps for $R-MBA_2PbI_4$ with σ^+pump and σ^+probe with Lorentzian fitting of the 3 peaks using 3 Lorentzian functions. GSB accounts for Ground State Bleach and ESA are the 2 Excited State Absorption peaks. On the lower right corner time evolution of the peak areas is tracked.

time evolution of the Lorentzian peak areas is observed and can be noticed how with longer probe delays the populations slowly get back to zero. The drastic changes in the peak areas at really long times are due artifacts in the measurement: at longer time delays the pump-probe alignment can change and also significantly less measurements are taken at longer times hence more error.

4.4 Spin Lifetimes

As aforementioned, polarized light causes the transitions to be spin dependent. Therefore polarized light causes a disequilibrium on the population of the excited spin states $(+\frac{1}{2}, -\frac{1}{2})$, the amount of time needed for the two populations to equilibrate is known as the spin lifetime.

When pump and probe have the same polarization we are exciting and "looking" at the same spin state. When cross polarization is used we are observing the amount of electrons that have flipped from one spin state to the other (spin flip). Equation 4.1 computes this difference of intensities between the two probes and allows for the calculation of spin lifetimes [26].

$$S(t) = I\sigma_+\sigma_+(t) - I\sigma_+\sigma_-(t) \tag{4.1}$$

In Figure 4.5 the spin lifetimes at the GSB (505 nm) are computed. GSB peak signal is chosen as the wavelength to study because it is in the excitonic resonance energy where the more visible changes on the spin recombination will be seen. The signal S(t) is the difference of intensity at time t when co-circular pump-probe and counter-circular pump-probe is used. This results in the data points seen in Figure 4.5 giving an exponential decay thus an exponential function will be used for fitting. The model used was an analytical convulution of a single exponential decay with a Gaussian IRF (See Annex 6).

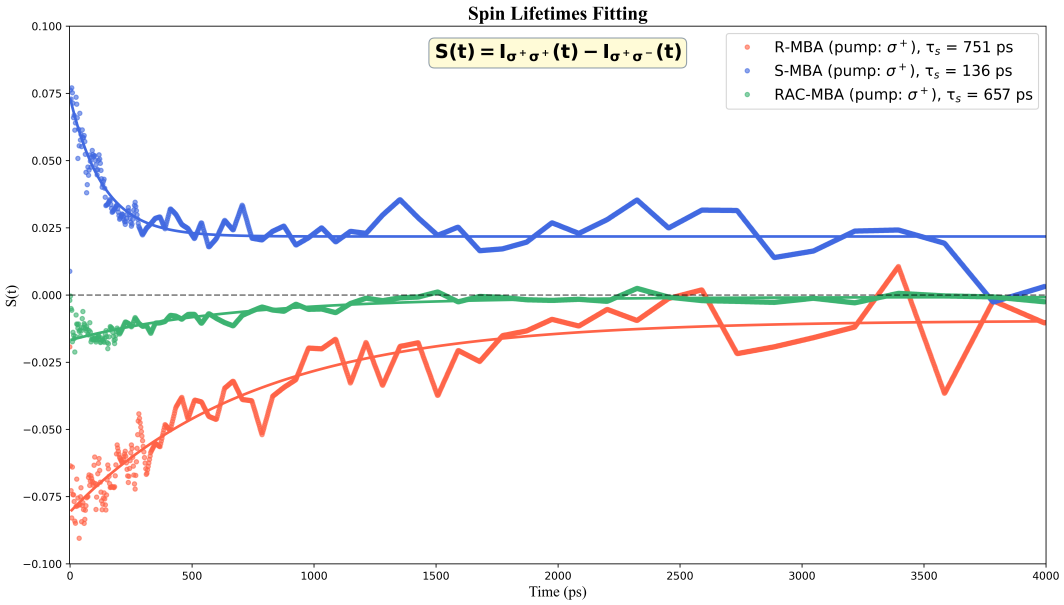

Figure 4.5: Spin Lifetimes fit at 505nm for the samples. Fluence is $8\mu J/cm^2$

In Figure 4.5 the fitted spin lifetimes are shown. R and S isomer present opposite behavior and the racemic counterpart shows little to no probe helicity nature. $S-MBA_2PbI_4$ presents a spin recombination lifetime of $136 \pm 9\ ps$ with a positive signal meaning that it is more susceptible to $\sigma+$ probe (recall that $\sigma+$ and $\sigma-$ are a conventionality). Notice how the signal does not reach zero, there is a long-time baseline offset of $C = 0.02$. Ideally there should be no offset since fluence was set to be the same but artifacts on the measurements (laser power fluctuations, small differences on the fluence, microstructure differences) make this offset. The lifetimes are way shorter that the once's reported in literature [39] but the experimental conditions also differ: compare 480 nm excitation and $8\mu J/cm^2$ fluence with Yang et al. 450 nm pump and $2.02\mu J/cm^2$. Also they used a bi-exponential model for fitting whereas with our data a mono-exponential fitting was more appropriate: we only consider one spin recombination movement hence only one spin lifetime to fit.
$R-MBA_2PbI_4$ shows a lifetime of $751 \pm 20\ ps$ with an offset of $C = -0.001$, longer than the 497 ps reported in Yang et al. The $S(t)$ signal for $R-MBA_2PbI_4$

presents oscillations on the shorter time frames where as its counter part S does not. Taking a deeper look at the TA spectra for R, one can see how, as opposite from S and racemic samples, R presents an increase if signal in the GSB after time zero followed by a decreases, where as for S and racemic there is only a decrease in the peak area after excitation. This difference is observed independent of the polarization used suggesting that is not a spin-dependent behavior. The intensity minima was tracked for the first 200 ps (See Figure 4.4), on Table 4.1 the intensity minimum's and times were tracked and 2 patterns observed: for same pump-probe polarization the minima was at an average of 25 ps but for counter pump-probe polarization the minima was at 35 ps. The fact that these time minima are same for right or left polarization denotes that this is not a spin polarization property. The longer lifetime with these differences in the photo-physics could be due to some difference photo-physical difference of the R isomer or perhaps some sample difference. New samples and measurements would be needed to assess if this is a photo-physical property of the R isomer or some experimental issue.

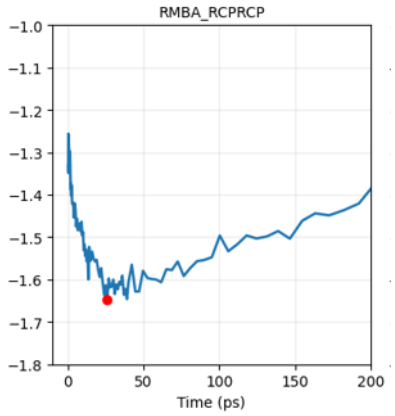

Figure 4.6: TA signal at GSB peak for $R - MBA_2PbI_4$ using $\sigma + \sigma +$ for the first 200 ps. Red dot indicates the minima intensity value

Taking a qualitative look at the racemic signal one can see that it presents little to non polarization dependent behavior. The racemic mixture presents small S(t) signal with a lifetime of 657 ± 15 ps. Ideally the signal should be zero since there should be no spin flip since both spin state populations should be populated equally but since the racemic sample is made by a mixture of R and S its possible that in the local domain the percentages are not fully fifty-fifty, hence some spin recombination. The spin lifetime being close to the R isomer could be due to racemic mixture having more R character in the excited section: notice also the negative S(t), behaving like the R isomer indicating more presence of R domain. For a better understanding of the racemic sample, multiple samples should be measured to account if this is a local domain result or intrinsic to the racemic mixture.

Table 4.1: Intensity minima for $R-MBA_2PbI_4$ data sets with different pump-probe polarization. Time minima was tracked

Data set polarization	$I_{(t=min)}$	**Time(ps)**
$\sigma+$ – $\sigma+$	-1.65	25.95
$\sigma-$ – $\sigma-$	-1.6	23.96
$\sigma+$ – $\sigma-$	-1.43	33.96
$\sigma-$ –$\sigma+$	-1.7	35.90

The big oscillations at longer times ($>$ 2000 ps) are due to noise in the measurements and the fact that very few time points are taken for a longer time frame (from 40 ps onward the time points are set in a logarithmic scale).
Although this method is good for assessing the polarization-dependent behavior of the samples there are still some open questions regarding the accuracy of these results. On the next section we propose a more complex method for acquiring the spin lifetimes.

4.5 Kinetic Model

On the previous section we have obtained the spin lifetimes by intensity difference when different probes are used. This method has some assumptions though: it assumes that all intensity difference comes from spin recombination and also that there is a 100% polarization when a certain helicity is being used.
On this next section we propose a new model to quantify the spin recombination rates through the kinetic constants. We will study how the carrier density population decays at the GSB peak wavelength. Firstly, intensity signal from TA needs to be converted to carrier density ($\frac{carriers}{cm^2}$) for the constants to have reasonable units and then be able to convert to spin lifetimes. In Annex 6 the full break down of the carrier densities is shown.
Approach for the kinetic model was to start simple and build up as complexity was needed. In Figure 4.7 a scheme of the kinetic processes considered after excitation is shown.

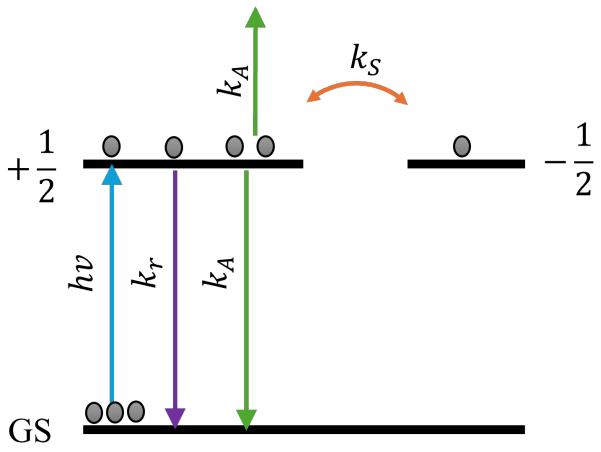

Figure 4.7: Scheme of the kinetic model used. GS represents the ground state, the arrow in blue represents the excitation to its excited state after a photon is absorbed. $+\frac{1}{2}$ and $-\frac{1}{2}$ refer to the two spin states. k_r is the excitonic recombination rate, k_A is the Auger-Meitner recombination rate, and k_s is the spin recombination rate.

The kinetic equation has an exciton recombination rate (k_r): after excitation the exciton formed will recombine and the electron will go back to the valance band [25]. k_A is the Auger-Meitner[1] when an electron-hole recombination transfers its energy to a third carrier (either another electron or hole), which is then excited to a higher energy state and eventually loses that energy as heat through phonon emission[4].Lastly, k_s is the spin recombination rate, which will be the focus term on our work. From kinetics we know that the lifetime of a specie its the inverse of the kinetic rate (given its a first order rate). Hence we can connect the spin lifetimes with its kinetic rate and vice-versa by:

$$\tau_s = \frac{1}{k_s} \tag{4.2}$$

Equation 4.3 shows the carrier population (N) decay. Notice that we use two carrier populations named (N_+ and N_-). Even though circularly polarized light is used we can not ensure 100% polarization of the excited states. Two coupled equations are used where the carrier density for both excited states is tracked. A polarization[2] (P) term is added (Equation 4.4) linking the two populations to the total carrier density. Notice the last term in both equations which is surplus term because it accounts for the electrons moving from the other spin state to that one. Having

[1]We use the term Auger-Meitner to recognize Lisa Meitner's contribution to the effect and being the first one to observe it. For more information on Meitner's work and life please refer to [9] [7].

[2]The term polarization will be refereed as how much population of each state we have, a percentage. Not to be confused with polarity of a molecule or polarization of light.

a two population model raises consequently raises the question: how much of each spin state is populated ?

$$\begin{aligned} \frac{dN_+}{dt} &= -k_r N_+ - k_A N_+^2 - k_S N_+ + k_S N_- \\ \frac{dN_-}{dt} &= -k_r N_- - k_A N_-^2 - k_S N_- + k_S N_+ \end{aligned} \tag{4.3}$$

$$N_{total}(t) = N_+ P \ + \ N_-(t)(1-P) \tag{4.4}$$

Although CPL is used, retardation error on the different optical parts of the setup can make it that the light is not fully circularly polarized and its degree of circular polarization to not be 100% therefore both carrier populations (N_+ and N_-) to be excited. Experimentally with TA is not possible to know this P value. A polarization sweep was done to find the best P values for fitting (See annex 6). The best fit was found with a polarization distribution between the two populations of 67% and 33% which matches with the Clebsch-Gordan coefficients for angular momentum coupling[13]. For racemic sample P value is set at 50% given that both states should be populated equally. Also $\sigma+$ and $\sigma-$ pump data sets were fit separately since for S and RAC, TA was measured on different occasions and TA spectra for different pump polarizations showed different intensity signals therefore fitting them separately showed better fittings. The fitting time window was set between 0 and 4000ps because at longer timescales we had way less data points and also they introduce more noise and less relevance, the main kinetic features are found in the short times.

Table 6.1 shows the initial carrier densities calculated for each of the samples (See Annex 6). On Figure 4.8 one can see how the different data sets present different

Table 4.2: Initial carrier density obtained from the fluence and absorption spectra.

	Initial carrier density($\frac{carriers}{cm^2}$)
R	8.66×10^{12}
S	7.17×10^{12}
RAC	7.49×10^{12}

decays, meaning different dynamics. Given that we have 3 constants to find, many combination of values can give a good fit, hence some bounds were put on the fitting parameters so the results had physical meaning (See Annex 6).

On Table 4.3 the kinetic constants obtained are shown. k_r is the exciton recombination process back to ground state, since this process does not depend on the spin state, it should be the same regarding polarization configuration. k_A depends on the carrier density but does not bother about their spin state so this constant should not depend on the polarization configuration either. Notice how k_a stays consistent for all samples and polarizations confirming the independence of polarization and

spin to this process. The difference of values for k_r and k_A si due to fitting artifacts given the differences in the experimental conditions.
See in Figure 4.8 the carrier decay for $R - MBA_2PbI_4$ how the decays for R with σ+pump are different for different probes. $\sigma+$ probe shows a higher increase in population after excitation. This difference in the data sets makes the fitting between them more complicated. We obtain a recombination lifetime of 650 ns when $\sigma+$ pump is used versus 193 ns when $\sigma-$ pump is used. The Auger-Meitner constant is almost identical for both polarizations. It shows that $R - MBA_2PbI_4$ responds to faster dynamics when $\sigma+$ pump is used. Continuing with k_r and k_A analysis, S sample shows consistent results for both pump helicities with a recombination lifetime of 17 ns and 31 ns when $\sigma+$ pump and $\sigma-$ pump are used, showcasing way faster rates than its enantiomer. Notice in Figure 4.9 how the fitting for $\sigma+$ pump is not optimal given that the two samples showcase different decays, specially in the 0-1000 ps range, underlying different photophysics and perhaps fitting one set of constants for these two datasets is not optimal but methodology was kept the same for all 3 samples. Its Auger-Meitner terms are consistent with both pumps. Racemic sample shows recombination lifetime of 56ns and 63ns respectively and consistent k_A values.
Moving on to the spin recombination constants, in Table 4.3 the spin constants (k_S) along with its spin lifetimes are shown. Notice how both R and S present very similar constants (its initial conditions for fitting where set the same) given that this lifetime addresses the same physical feature but in opposite directions. R and S are mirror images of each other, the handiness controls the sign of the spin polarization but not the rate. These two enantiomers have the same chemical and crystalline structure so its expected that the spin relaxation mechanism be the same, implying same amount of time. There is still a difference on the results when different pumps are used: compare 123 ps to 249 ps for R sample highlighting how the two polarizations have different relaxation pathways.
Racemic mixtures has faster relaxation rates with a lifetime of 46 ps and 43 ps. Because it is a racemic mixture has 50% populated each spin state, the time that it requires for both states to equilibrate in population is way shorter. Ideally it would be zero, given both states should be equally populated, but due to the sample probably not being fully racemic there is still some spin to equilibrate.

Therefore, with this kinetic model we have been able to study the carrier dynamics of R, S- and RAC-MBA_2PbI_4 and propose a model to explain the population decay. By tracking two coupled spin populations simultaneously, the model goes beyond the assumptions of the helicity-difference method and provides explicit rate constants for excitonic recombination (k_r), Auger-Meitner recombination (k_A), and

spin relaxation (k_s). The Auger-Meitner constants are consistent across all samples and pump-probe polarizations, confirming it is a chirality-independent process and proving the physical meaning behind the model. The spin lifetimes extracted for R and S are similar in magnitude, as expected for mirror structures where the spin relaxation mechanism is the same but with opposite handedness, while the racemic mixture shows a significantly shorter spin lifetime given that the two spin states are already equally populated.

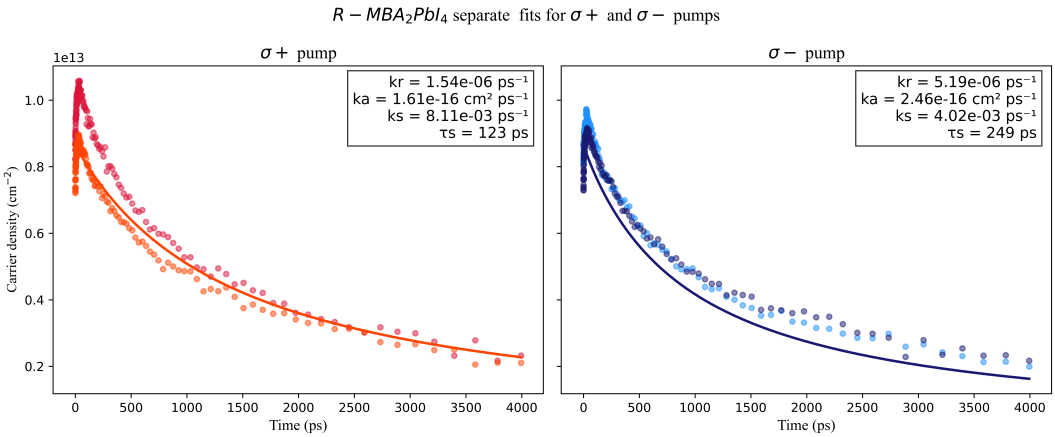

Figure 4.8: Kinetic model fitting for $R-MBA_2PbI_4$ fitting $\sigma+$ and $\sigma-$ pump data separately. k_r is the excitonic recombination rate, k_A is the Auger-Meitner effect constant and k_s is the spin recombination rate. In darker red $\sigma+\sigma+$ pump-probe and in orange $\sigma+\sigma-$ pump-probe. In lighter blue $\sigma-\sigma-$ and in darker blue $\sigma-\sigma+$. P value is 0.67 and 0.33 for N_+ and N_-.

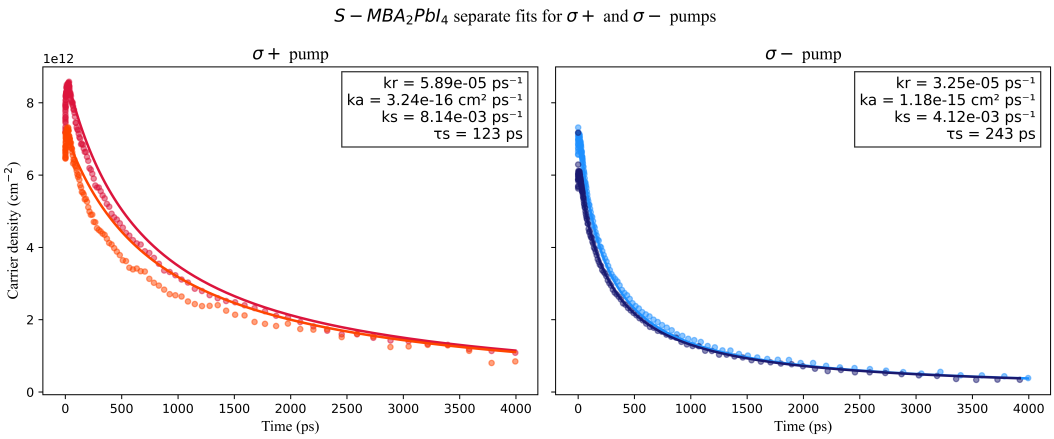

Figure 4.9: Kinetic model fitting for $S - MBA_2PbI_4$ fitting $\sigma+$ and $\sigma-$ pump data separately. k_r is the excitonic recombination rate, k_A is the Auger-Meitner effect constant and k_s is the spin recombination rate. In darker red $\sigma + \sigma+$ pump-probe and in orange $\sigma + \sigma-$ pump-probe. In lighter blue $\sigma - \sigma-$ and in darker blue $\sigma - \sigma+$. P value is 0.33 and 0.67 for N_+ and N_-.

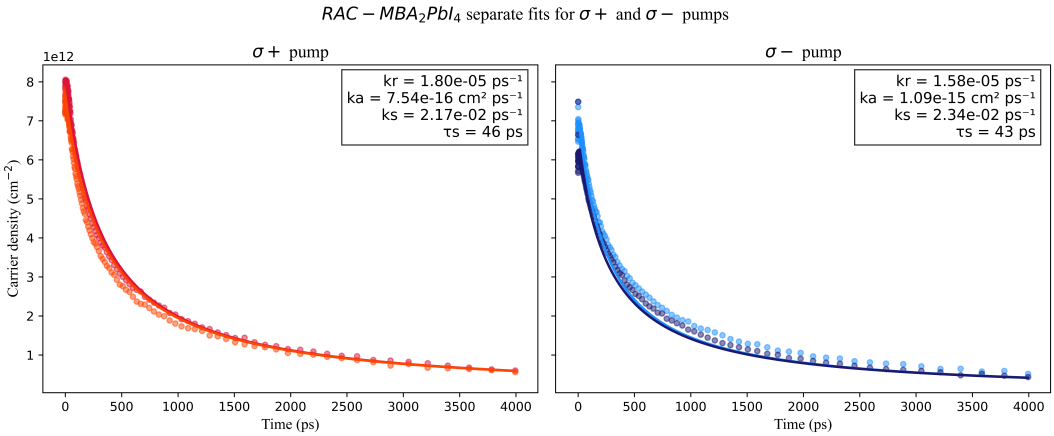

Figure 4.10: Kinetic model fitting for $RAC - MBA_2PbI_4$ fitting $\sigma+$ and $\sigma-$ pump data separately. k_r is the excitonic recombination rate, k_A is the Auger-Meitner effect constant and k_s is the spin recombination rate. In darker red $\sigma + \sigma+$ pump-probe and in orange $\sigma + \sigma-$ pump-probe. In lighter blue $\sigma - \sigma-$ and in darker blue $\sigma - \sigma+$. P value is 0.50 and 0.50 for N_+ and N_-.

Table 4.3: Kinetic model parameters extracted from the coupled rate equation fitting of the carrier density traces for R-, S-, and RAC-MBA_2PbI_4 under σ^+ and σ^- circularly polarized pump excitation. k_r is the excitonic recombination rate, k_A is the Auger-Meitner recombination coefficient, k_s is the spin relaxation rate, and $\tau_s = 1/k_s$ is the spin lifetime.

Sample	Pump	k_r (ps^{-1})	k_A (cm^2 ps^{-1})	k_s (ps^{-1})	τ_s (ps)
R-MBA_2PbI_4	σ^+	1.53×10^{-6}	1.48×10^{-16}	8.11×10^{-3}	123
	σ^-	5.18×10^{-6}	1.49×10^{-16}	4.02×10^{-3}	249
S-MBA_2PbI_4	σ^+	5.89×10^{-5}	3.24×10^{-16}	8.14×10^{-3}	123
	σ^-	3.25×10^{-5}	1.18×10^{-15}	4.12×10^{-3}	243
RAC-MBA_2PbI_4	σ^+	1.80×10^{-5}	7.54×10^{-16}	2.17×10^{-2}	46
	σ^-	1.58×10^{-5}	1.09×10^{-15}	2.34×10^{-2}	43

4.6 Comparison of Spin Lifetimes: Helicity-Difference Method vs Kinetic Model

On the previous sections two independent methods have been used to extract the spin lifetimes of R-, S- and RAC-MBA_2PbI_4. Table 4.4 summarizes the results from both methods side by side.

Table 4.4: Comparison of spin lifetimes extracted by the helicity-difference method and the kinetic model for each sample and pump helicity.

Sample	Helicity-Diff. τ_s (ps)	Kinetic Model τ_s σ^+ (ps)	Kinetic Model τ_s σ^- (ps)
R-MBA_2PbI_4	751	123	249
S-MBA_2PbI_4	136	123	243
RAC-MBA_2PbI_4	657	46	43

The kinetic model provides consistent results from both pump helicities. The fastest spin relaxation comes from the racemic sample, as expected, and R and S show a longer spin lifetime, suggesting that the chiral organic ligand prolongs the spin lifetime. On the other hand, the helicity-difference method does not give the same ordering: the racemic sample shows a longer lifetime than the S sample. As discussed above, this could be due to the signal being very close to the noise level, or the fact that the sample is not fully racemic. Still, both methods show the influence of CISS on the decay and a polarization dependence, thus we can say that

the chirality transfer from MBA leaves a footprint on the decay pathways of the perovskite, confirming the manifestation of the CISS effect on the spin dynamics of R-, S-, and RAC-MBA_2PbI_4.

The key difference in the results of the two methods arises from what is actually accounted as spin lifetime. In the helicity-difference method, the spin lifetime is extracted from the difference in decay between co-circular and counter-circular probe configurations, and it is assumed that all the difference in decay comes from spin-dependent phenomena and that 100% spin population is created by the pump.

The kinetic model deconstructs the decay into different contributions and only one of them (k_s)determines the spin lifetime. Contrary to the helicity-difference method, it does not assume 100% polarization: instead, the degree of spin polarization P is an explicit parameter of the model consistent with the Clebsch-Gordan coefficients for angular momentum coupling [13].

The main difference between the two methods is therefore what is considered as the spin lifetime and which model is used to extract it. A review by Huang et al.[17] showed that different spin lifetimes are obtained for the same material when different techniques are implemented, highlighting that spin lifetime is inherently a model-dependent quantity. Yang et al.[39], who studied the same material, used a bi-exponential fitting model without explicitly discussing the physical justification for the two components.

Thus with both methods the CISS effect is observed on the results but absolute values differ. Future work (See Chapter 6) would be needed to asses the veracity of the new kinetic model and the question if CISS polarizes 100% of the spin still to be answered.

Chapter 5

Conclusion

In this project we have seen how spin dynamics of R-, S-, and RAC-MBA_2PbI_4 are affected by the CISS effect. Circularly Polarized Transient Absorption has proven to be a powerful tool for uncovering the spin dynamics of these materials. The R and S enantiomers have shown to have distinct spin dynamics that its racemic counterpart. The two methods used to account for spin lifetimes have proven the influence of the chiral spacer MBA on the dynamics but its results differ on absolute values proving that spin lifetime is a model-dependent quantity [35]. The proposed kinetic model separates the different processes after excitation and accounts for a polarization parameter P consistent with the Clebsch-Gordan coefficients for angular momentum coupling.

Together, these results establish new insights into the quantification of spin relaxation rates in chiral hybrid lead halide perovskites and highlight the need for standardizing measurement and modelling approaches in this rapidly growing field.

Chapter 6

Future Work

This thesis has established two complementary methods for extracting spin lifetimes in chiral 2D perovskites and identified several open questions that future work should address.

The kinetic model proposed here relies on three rate constants: k_r, k_A, and k_s. While the Auger-Meitner constants show good consistency across samples and polarizations, k_r shows some variation between pump helicities that is attributed to fitting artefacts from different experimental conditions. A natural next step would be to perform fluence-dependent CPTA measurements: varying the pump fluence over a wider range would allow k_r and k_A to be independently constrained before fitting the spin dynamics. Complementary time-resolved photoluminescence (TRPL) measurements would provide an independent measurement of the radiative lifetime [29], which can be directly compared to $1/k_r$ from the kinetic model and serve as a strong external validation.

For the R-MBA_2PbI_4 sample, the anomalous GSB peak rise observed after excitation remains an open question. As discussed in the results, this behaviour is independent of the pump-probe polarization configuration, suggesting it is not a spin-dependent effect. However it is not clear whether this is an intrinsic photophysical property of the R isomer or an experimental artifact from the specific thin film sample used. To resolve this, new R-MBA_2PbI_4 samples should be synthesized and measured under the same conditions. If the build-up is reproduced consistently across samples, it would point to a genuine photophysical difference between R and S enantiomers worth investigating further, perhaps related to differences in crystal packing or exciton formation dynamics. If it is not reproducible, it would confirm a sample-specific issue and the 751 ps spin lifetime from Method 1 should be treated with caution and the new spin lifetime calculated.

Temperature-dependent measurements would be particularly valuable for understanding the spin relaxation mechanisms present in these materials given that the main spin relaxation mechanisms have different temperature dependences: the

DP rate decreases with increasing temperature while EY increases with temperature [35]. Fluence-dependent measurements would also be beneficial for a deeper understanding and influence on the Auger-Meitner term and also how does fluence affect the spin relaxation mechanisms.
Together these experiments would provide a much more complete picture of spin relaxation in (R/S/RAC-MBA)$_2$PbI$_4$ and establish whether the kinetic model proposed in this thesis captures all the relevant physics or requires further development.

Bibliography

[1] Jihoon Ahn, Sunihl Ma, Ji-Young Kim, Jihoon Kyhm, Wei Wang, Jan Seidel, Nicholas A. Kotov, and Jooho Moon. Chiral 2d organic inorganic hybrid perovskite with circular dichroism tunable over wide wavelength range. *Journal of the American Chemical Society*, 142(9):4206–4212, 2020.

[2] F. Almog, M.S. Bradley, and V. Bulovic . The lorentz oscillator and its applications (mit opencourseware).

[3] Steven S. Andrews and James Tretton. Physical principles of circular dichroism. 97(12):4370–4376.

[4] A. R. Beattie and P. T. Landsberg. Auger effect in semiconductors. *Proceedings of the Royal Society of London. A. Mathematical and Physical Sciences*, 249(1256):16–29, January 1959. _eprint: https://royalsocietypublishing.org/rspa/article-pdf/249/1256/16/51398/rspa.1959.0003.pdf.

[5] Pratik Bharat Bhagwat and Tönu Pullerits. Time-resolved excitons and spin dynamics in chiral 2d lead halide.

[6] J.-C. Blancon, A. V. Stier, H. Tsai, W. Nie, C. C. Stoumpos, B. Traoré, L. Pedesseau, M. Kepenekian, F. Katsutani, G. T. Noe, J. Kono, S. Tretiak, S. A. Crooker, C. Katan, M. G. Kanatzidis, J. J. Crochet, J. Even, and A. D. Mohite. Scaling law for excitons in 2D perovskite quantum wells. *Nature Communications*, 9(1):2254, June 2018.

[7] Britannica Editors. Lise meitner, November 2025.

[8] Robert P. Cameron, Jörg B. Götte, Stephen M. Barnett, and Alison M. Yao. Chirality and the angular momentum of light. 375(2087):20150433.

[9] Brenda Laster Ruth Sime Demetrios Matsakis, Anthea Coster. A renaming proposal: "the auger–meitner effect". *Physics Today*, 2019.

[10] M. I. Dyakonov and V. I. Perel. Current-induced spin orientation of electrons in semiconductors. *Physics Letters A*, 35(6):459–460, 1971.

[11] R. J. Elliott. Theory of the effect of spin-orbit coupling on magnetic resonance in some semiconductors. *Physical Review*, 96(2):266–279, 1954.

[12] Ferdinand Evers, Amnon Aharony, Nir Bar-Gill, Ora Entin-Wohlman, Per Hedegård, Oded Hod, Pavel Jelinek, Grzegorz Kamieniarz, Mikhail Lemeshko, Karen Michaeli, Vladimiro Mujica, Ron Naaman, Yossi Paltiel, Sivan Refaely-Abramson, Oren Tal, Jos Thijssen, Michael Thoss, Jan M. Van Ruitenbeek, Latha Venkataraman, David H. Waldeck, Binghai Yan, and Leeor Kronik. Theory of chirality induced spin selectivity: Progress and challenges. 34(13):2106629.

[13] David Giovanni, Hong Ma, Julianto Chua, Michael Grätzel, Ramamoorthy Ramesh, Subodh Mhaisalkar, Nripan Mathews, and Tze Chien Sum. Highly Spin-Polarized Carrier Dynamics and Ultralarge Photoinduced Magnetization in CH3NH3PbI3 Perovskite Thin Films. *Nano Letters*, 15(3):1553–1558, March 2015.

[14] Ji Hao, Haipeng Lu, Lingling Mao, Xihan Chen, Matthew C. Beard, and Jeffrey L. Blackburn. Direct detection of circularly polarized light using chiral copper chloride–carbon nanotube heterostructures. 15(4):7608–7617.

[15] C. R. Harris et al. Array programming with NumPy. *Nature*, 585:357–362, 2020.

[16] Hartmut Haug and Stephan W. Koch. *Quantum theory of the optical and electronic properties of semiconductors*. World Scientific, 4. ed., repr edition.

[17] Wenjin Huang, Zhiruo Zhou, Sang Hyun Nam, Qiong Chen, Jingying Wang, Zhiyao Zeng, Chenglong Ge, Ying Li, Jifei Wang, Young-Hoon Kim, and Yaxin Zhai. Spin lifetime in hybrid organic–inorganic perovskites: Mechanisms, measurements, and prospects for spintronic applications. *The Journal of Physical Chemistry Letters*, 16(20):5109–5120, 2025.

[18] Manoj K. Jana, Ruyi Song, Haoliang Liu, Dipak Raj Khanal, Svenja M. Janke, Rundong Zhao, Chi Liu, Z. Valy Vardeny, Volker Blum, and David B. Mitzi. Organic-to-inorganic structural chirality transfer in a 2D hybrid perovskite and impact on Rashba–Dresselhaus spin-orbit coupling. *Nature Communications*, 11:4699, 2020.

[19] Menghui Jia, Jie Kong, Huangmei Zhou, Jinquan Chen, Sanjun Zhang, and Meng Zhou. Transient absorption spectroscopy: Probing the ultrafast dynamics in nanomaterial complex systems. In Nandakumar Kalarikkal, Rodolphe Antoine, Sabu Thomas, and Padiyakkuth Nideesh, editors, *Laser-based Techniques for Nanomaterials*, pages 262–286. Royal Society of Chemistry.

[20] LibreTexts. 6.06: Chirality in organic chemistry, 2026. Accessed: 2026-05-27.

[21] Haipeng Lu, Jingying Wang, Chuanxiao Xiao, Xin Pan, Xihan Chen, Roman Brunecky, Joseph J. Berry, Kai Zhu, Matthew C. Beard, and Zeev V. Vardeny. Spin-dependent charge transport through 2d chiral hybrid lead-iodide perovskites. *Science Advances*, 5(12):eaay0571, 2019.

[22] Sunihl Ma, Young-Kwang Jung, Jihoon Ahn, Jihoon Kyhm, Jeiwan Tan, Hyungsoo Lee, Gyumin Jang, Chan Uk Lee, Aron Walsh, and Jooho Moon. Elucidating the origin of chiroptical activity in chiral 2D perovskites through nano-confined growth. *Nature Communications*, 13(1):3259, June 2022.

[23] Urmila Makhija, Parikshit Kumar Rajput, Pavithra Parthiban, and Angshuman Nag. Effect of film morphology on circular dichroism of low-dimensional chiral hybrid perovskites. *The Journal of Chemical Physics*, 160(2):021102, January 2024.

[24] Lingling Mao, Constantinos C. Stoumpos, and Mercouri G. Kanatzidis. Two-dimensional hybrid halide perovskites: Principles and promises. *Journal of the American Chemical Society*, 141(3):1171–1190, 2019.

[25] Rebecca L. Milot, Rebecca J. Sutton, Giles E. Eperon, Amir Abbas Haghighirad, Josue Martinez Hardigree, Laura Miranda, Henry J. Snaith, Michael B. Johnston, and Laura M. Herz. Charge-carrier dynamics in 2d hybrid metal–halide perovskites. 16(11):7001–7007.

[26] R. Naaman and David H. Waldeck. Chiral-induced spin selectivity effect. 3(16):2178–2187.

[27] Ron Naaman and David H. Waldeck. Spintronics and chirality: spin selectivity in electron transport through chiral molecules. *Annual Review of Physical Chemistry*, 66:263–281, 2015.

[28] R. Nave. Quarter-wave plate. `http://hyperphysics.phy-astr.gsu.edu/hbase/phyopt/quarwv.html`. HyperPhysics, Georgia State University, accessed 2026-05-26.

[29] Jonas Physik, Lin Jiang, Moritz H. Futscher, and Bruno Ehrler. PEARS: A web tool for fitting time-resolved photoluminescence decays of perovskite materials. *Journal of Chemical Information and Modeling*, 63(12):3686–3693, 2023.

[30] K. Ray, S. P. Ananthavel, D. H. Waldeck, and R. Naaman. Asymmetric scattering of polarized electrons by organized organic films of chiral molecules. *Science*, 283(5403):814–816, 1999.

[31] Marcello Righetto, David Giovanni, Swee Sien Lim, and Tze Chien Sum. The photophysics of Ruddlesden-Popper perovskites: A tale of energy, charges, and spins. *Applied Physics Reviews*, 8(1):011318, March 2021.

[32] Bahaa E A Saleh and Malvin Carl Teich. FUNDAMENTALS OF PHOTONICS.

[33] Daniel B. Straus and Cherie R. Kagan. Photophysics of two-dimensional semiconducting organic–inorganic metal-halide perovskites. *Annual Review of Physical Chemistry*, 73:Submitted, 2021.

[34] P. Virtanen et al. SciPy 1.0: fundamental algorithms for scientific computing in Python. *Nature Methods*, 17:261–272, 2020.

[35] Igor Žutić, Jaroslav Fabian, and Sankar Das Sarma. Spintronics: Fundamentals and applications. *Reviews of Modern Physics*, 76(2):323–410, 2004.

[36] David H. Waldeck et al. Chirality-induced spin selectivity in chiral hybrid organic-inorganic perovskite semiconductors. *Annual Review of Physical Chemistry*, 2024.

[37] Jingying Wang, Haipeng Lu, Xin Pan, Junwei Xu, Haoliang Liu, Xiaojie Liu, Dipak R. Khanal, Michael F. Toney, Matthew C. Beard, and Z. Valy Vardeny. Spin-dependent photovoltaic and photogalvanic responses of optoelectronic devices based on chiral two-dimensional hybrid organic–inorganic perovskites. 15(1):588–595.

[38] Wikipedia contributors. Perovskite (structure) — wikipedia, the free encyclopedia, 2026. [Online; accessed 24-May-2026].

[39] Yubo Yang, Wenli Su, Xiaofan Jiang, Pengyu Zhang, and Wenkai Zhang. Lattice chirality prolongs exciton spin depolarization in 2d perovskites by enhanced exciton-phonon coupling. 14(9):e03363.

[40] Xiaohui Yao and Chao Liang. Chirality and the angular momentum of light. *Philosophical Transactions of the Royal Society A*, 375(2087):20150433, 2017.

Annex A Spin Lifetime Extraction

A.1 Carrier Density Calculation

The initial carrier density N_0 is calculated from the pump fluence F and the sample absorbance at the pump wavelength $\lambda_{\text{pump}} = 480\,\text{nm}$:

$$N_0 = \frac{F\left(1 - 10^{-\text{Abs}_{480}}\right)}{E_{\text{photon}}}, \qquad E_{\text{photon}} = \frac{hc}{\lambda_{\text{pump}}}, \tag{6.1}$$

where h is Planck's constant, c is the speed of light, and Abs_{480} is the measured absorbance at 480 nm. The film is treated as two-dimensional, so N_0 is an areal density (carriers cm^{-2}). For a pump fluence of $F = 7.89\,\mu\text{J}\,\text{cm}^{-2}$, the photon energy at 480 nm is $E_{\text{photon}} = 4.14 \times 10^{-19}\,\text{J}$, yielding the initial carrier densities listed in Table 6.1.

Table 6.1: Initial carrier density calculated from absorption spectra measurements at the pump wavelength (480 nm) and a fluence of $F = 7.89\,\mu\text{J}\,\text{cm}^{-2}$.

Sample	Abs_{480}	T_{480}	N_0 (cm^{-2})
R-MBA_2PbI_4	0.263	0.546	8.67×10^{12}
S-MBA_2PbI_4	0.205	0.624	7.16×10^{12}
RAC	0.217	0.601	7.48×10^{12}

A.2 Software Environment

All data processing and fitting were performed in Python 3 using the following libraries: `NumPy` [15] for numerical operations, `pandas` for data ingestion, `SciPy` [34] (`scipy.optimize.curve_fit` and `scipy.special.erfc`) for nonlinear least-squares optimisation, and `Matplotlib` for visualisation.

A.3 Construction of the Spin Signal $S(t)$

The spin-polarisation signal $S(t)$ was constructed as the helicity difference

$$S(t) = I_{\sigma^+\sigma^+}(t) - I_{\sigma^+\sigma^-}(t). \tag{6.2}$$

Before subtraction, both traces were interpolated onto a common uniform time axis using linear interpolation. The resulting $S(t)$ was normalised by the peak abso-

lute value of the total population signal ($I_{\sigma^+\sigma^+} + I_{\sigma^+\sigma^-}$), so that $S(t)$ represents the fractional spin polarisation relative to the total excited population, making results comparable across samples measured at different pump fluences.

A.4 Fitting Model

The spin lifetime was extracted by fitting $S(t)$ with the analytical convolution of a single-sided exponential decay $e^{-t/\tau}\,\Theta(t)$ with a Gaussian IRF of 1σ width s. This convolution yields

$$S(t) = C + \frac{A}{2}\exp\left(\frac{s^2}{2\tau^2} - \frac{t-t_0}{\tau}\right)\operatorname{erfc}\left(\frac{s}{\sqrt{2}\,\tau} - \frac{t-t_0}{\sqrt{2}\,s}\right), \tag{6.3}$$

where A is the spin-polarisation amplitude, $\tau \equiv \tau_s$ is the spin lifetime, t_0 is the pump-probe time zero, s is the 1σ width of the Gaussian IRF, and C is a long-time baseline offset. The complementary error function erfc arises naturally from the convolution integral and correctly accounts for the finite signal rise near t_0; without it, an instantaneous step model would underestimate τ_s. The baseline C absorbs any residual long-lived spin polarisation or detector drift that persists beyond the measurement window, and is independent of the amplitude normalisation applied during trace construction.

A.5 Fitting Procedure and Parameter Bounds

Nonlinear least-squares fitting was performed using `scipy.optimize.curve_fit`. The fit was applied over the time window $t \in [0,\, 4000]$ ps.

For each sample, initial parameter guesses were generated automatically from the data as follows:

- t_0: time of maximum absolute gradient of $S(t)$, approximating the signal onset.
- s: three times the median time step, clipped to $[0.05,\, 0.50]$ ps.
- A: difference between the maximum and long-time mean of $S(t)$.
- τ: 30 % of the total fitted time range, clipped to $[1,\, 1000]$ ps.
- C: mean of $S(t)$ over the final 20 % of the time axis, approximating the long-time baseline.

The physical bounds applied to the five free parameters $[C,\, t_0,\, s,\, A,\, \tau]$ are summarised in Table 6.2.

Table 6.2: Parameter bounds used in nonlinear least-squares fitting of $S(t)$ with the IRF-convolved model (Eq. 6.3).

Parameter	Physical meaning	Unit	Lower bound	Upper bound
C	Long-time baseline offset	(norm.)	-0.2	0.2
t_0	Pump–probe time zero	ps	0.0	1.0
s	IRF 1σ width	ps	0.01	1.0
A	Spin-polarisation amplitude	(norm.)	-1.0	1.0
τ_s	Spin lifetime	ps	0.1	800

For samples exhibiting coherent artefacts near $t = 0$, a small number of leading data points were excluded from the fit to prevent bias in the extracted τ_s. These points were retained in all figures for transparency.

A.6 Uncertainty Estimation

The 1σ uncertainty on each fitted parameter was obtained from the square root of the corresponding diagonal element of the covariance matrix C returned by `curve_fit`:

$$\delta\theta_i = \sqrt{C_{ii}}, \tag{6.4}$$

where θ_i denotes the i-th fitted parameter. This estimate assumes Gaussian noise and linearises the model around the optimal solution. The spin lifetime and its uncertainty are reported as $\tau_s \pm \delta\tau_s$ (1σ) throughout.

Annex B Computational Details for Kinetic Model Fitting

B.1 Software Environment

All kinetic modelling was performed in Python 3 using `NumPy` [15] for numerical operations, `pandas` for data loading, `SciPy` [34] for ODE integration (`scipy.integrate.solve_ivp`) and least-squares optimisation (`scipy.optimize.least_squares`), and `Matplotlib` for visualisation.

B.2 Carrier Density Conversion

The transient absorption (TA) signal ΔA is proportional to the excited carrier population. To convert it to an areal carrier density N (carriers cm^{-2}), the ground-state bleach (GSB) kinetic trace at $\lambda_{\mathrm{probe}} = 505\,\mathrm{nm}$ was extracted from each dataset. The initial carrier density N_0 was calculated from the pump fluence F and the sample absorbance at the pump wavelength $\lambda_{\mathrm{pump}} = 480\,\mathrm{nm}$:

$$N_0 = \frac{F\left(1 - 10^{-\mathrm{Abs}_{480}}\right)}{E_{\mathrm{photon}}}, \qquad E_{\mathrm{photon}} = \frac{hc}{\lambda_{\mathrm{pump}}}, \tag{6.5}$$

where h is Planck's constant, c is the speed of light, and Abs_{480} is the measured absorbance at 480 nm. A pump fluence of $F = 7.89 \times 10^{-6}\,\mathrm{J\,cm^{-2}}$ was used for all samples. The resulting initial carrier densities are listed in Table 6.1. The time-dependent carrier density trace $N(t)$ was obtained by scaling the TA kinetic trace so that $N(t=0) = N_0$:

$$N(t) = N_0 \cdot \frac{\Delta A(t)}{\Delta A(t=0)}. \tag{6.6}$$

B.3 Kinetic Rate Equations

The coupled ordinary differential equations (ODEs) governing the time evolution of the two spin populations N_+ and N_- are:

$$\begin{aligned} \frac{dN_+}{dt} &= -k_r N_+ - k_A N_+^2 - k_S N_+ + k_S N_- \\ \frac{dN_-}{dt} &= -k_r N_- - k_A N_-^2 - k_S N_- + k_S N_+, \end{aligned} \tag{6.7}$$

where k_r (ps^{-1}) is the monomolecular excitonic recombination rate, k_A ($\mathrm{cm}^2\,\mathrm{ps}^{-1}$) is the Auger–Meitner bimolecular recombination coefficient, and k_S (ps^{-1}) is the spin relaxation rate. The observable total carrier density is:

$$N_{\mathrm{total}}(t) = P \cdot N_+(t) + (1 - P) \cdot N_-(t), \tag{6.8}$$

where $P \in [0, 1]$ is the spin polarisation parameter defining the fractional population of the majority spin state at $t = 0$:

$$N_+(0) = P \cdot N_0, \qquad N_-(0) = (1 - P) \cdot N_0. \tag{6.9}$$

B.4 ODE Integration

The system of equations (6.7) was integrated numerically using `scipy.integrate.solve_ivp` with the `LSODA` method. The ODE was evaluated on the experimental time axis $t \in [0, 4000]\,\mathrm{ps}$ at the measured time points via the `t_eval` argument.

B.5 Spin Polarization Parameter P

The degree of spin polarization P cannot be directly measured from the TA experiment. To determine the optimal value, a polarization sweep was performed for each sample: the full fitting procedure was repeated for $P \in \{1.00,\ 0.90,\ 0.75,\ 0.67\}$ for the majority spin channel (with $1-P$ for the minority channel), and the resulting fits were compared visually and by residual cost. The best fits across all samples were obtained consistently at $P = 0.67$ for the majority spin channel and $P = 0.33$ for the minority channel. This 2:1 ratio is consistent with the Clebsch–Gordan coefficients (See Annex 6) for angular momentum coupling in a two-level spin system under circularly polarized excitation [13], where σ^+ excitation populates the $m_J = +\frac{1}{2}$ state with probability $|\langle +\frac{1}{2}|\hat{e}_+|-\frac{1}{2}\rangle|^2 = \frac{2}{3}$ and the $m_J = -\frac{1}{2}$ state with probability $\frac{1}{3}$. For the racemic sample, P was fixed at 0.50 since both spin states are expected to be equally populated.

B.5.1 Kinetic Fits for Different P Values

Note that opposite combinations of P values (e.g. 33%/67%) yield the same rate constants but with the spin populations interchanged. For the racemic mixture, no sweep was performed since equal populations ($P = 50\%$) are assumed by symmetry.

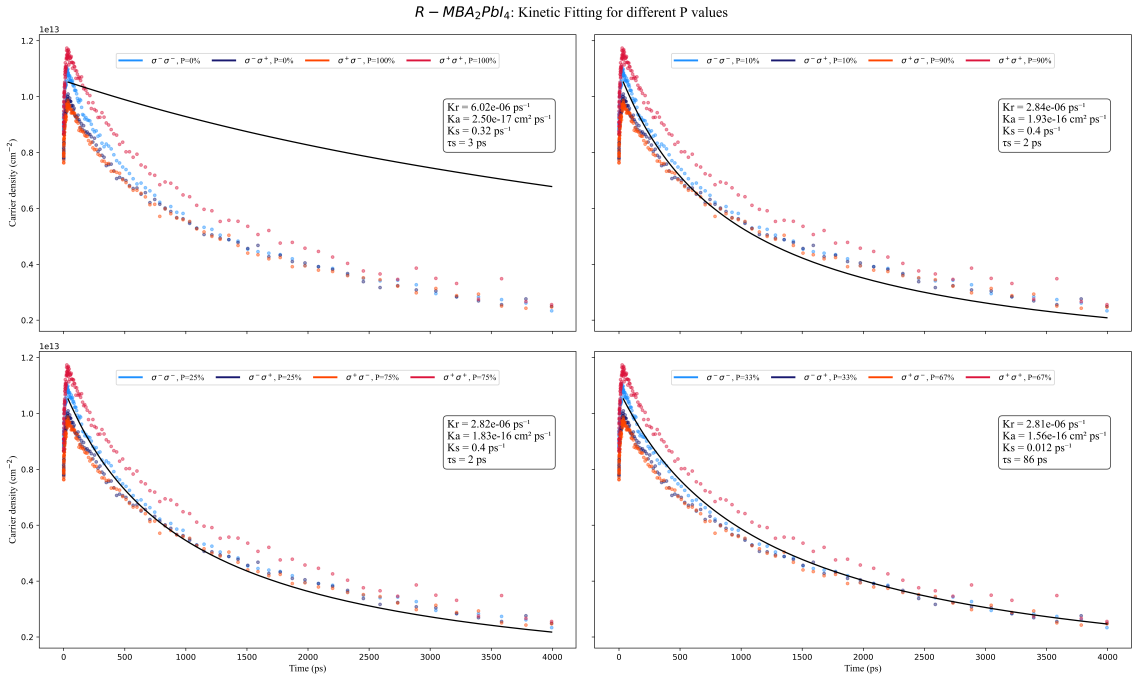

Figure 6.1: Polarization sweep for R-MBA_2PbI_4.

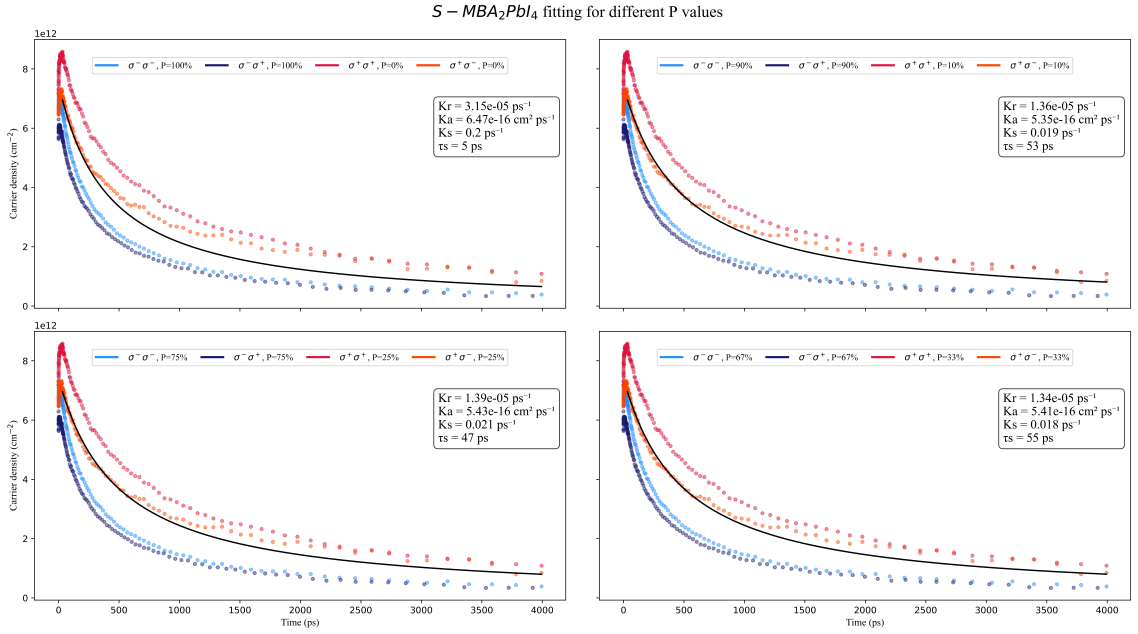

Figure 6.2: Polarisation sweep for S-MBA_2PbI_4.

B.6 Fitting Procedure

The three kinetic parameters $\theta = [k_r,\, k_A,\, k_S]$ were extracted by minimising the sum of squared residuals between the simulated $N_{\text{total}}(t)$ and the experimental carrier density traces.

The optimisation was performed using `scipy.optimize.least_squares` with the `soft_l1` robust loss function:

$$\hat{\theta} = \arg\min_{\theta} \sum_{i} \rho\left(\frac{[N_{\text{model}}(t_i;\, \theta) - N_{\text{exp}}(t_i)]^2}{f_s^2} \right), \tag{6.10}$$

where $\rho(z) = 2(\sqrt{1+z} - 1)$ is the soft-ℓ_1 function that down-weights outliers, and f_s is a scale factor set to 10^{11}–$10^{12}\,\text{cm}^{-2}$ (matching the carrier density scale) to ensure numerically well-conditioned residuals. The initial condition for each ODE integration was taken as the measured carrier density at the start of the fit window rather than the calculated N_0.

The fit window was $t \in [t_{\min},\, 4000]\,\text{ps}$, where $t_{\min}$ was set to the time of the carrier density peak (typically 30-60 ps after $t = 0$) to exclude the early-time rise.

B.7 Parameter Bounds

Physical bounds were applied to all three fitted parameters to prevent convergence to unphysical solutions. The bounds used are summarised in Table 6.3.

Table 6.3: Parameter bounds applied during kinetic model fitting.

Parameter	Physical meaning	Unit	Lower bound	Upper bound
k_r	Excitonic recombination rate	ps^{-1}	1.1×10^{-6}	5×10^{-4}
k_A	Auger–Meitner coefficient	$\text{cm}^2\,\text{ps}^{-1}$	2×10^{-20}	1×10^{-12}
k_S	Spin relaxation rate	ps^{-1}	1×10^{-5}	1×10^{-2}

The lower bound on k_r corresponds to a recombination lifetime of $\sim$900 ns, well beyond the measurement window; the upper bound corresponds to $\sim$2 ps, faster than exciton formation. The bounds on k_A span six orders of magnitude to accommodate the wide range of Auger coefficients reported for 2D perovskites. The bounds on k_S correspond to spin lifetimes between $\sim$100 ns and $\sim$100 ps, bracketing the physically expected range for spin relaxation in lead halide perovskites.

Annex C Clebsch–Gordan Coefficients

Clebsch–Gordan (CG) coefficients are the expansion coefficients of total angular momentum eigenstates in an uncoupled tensor product basis. They arise in the coupling of two angular momenta j_1 and j_2 into a total angular momentum J.

C.1 Uncoupled (Product) Basis

The uncoupled basis is formed by the tensor product of the individual angular momentum eigenstates:

$$|j_1, m_1\rangle \otimes |j_2, m_2\rangle, \qquad m_i = -j_i, -j_i + 1, \ldots, j_i.$$

This basis spans a space of dimension $(2j_1 + 1)(2j_2 + 1)$.

C.2 Coupled Basis

The coupled basis consists of simultaneous eigenstates of $\hat{J}^2$, $\hat{J}_z$, $\hat{j}_1^2$, and $\hat{j}_2^2$, denoted $|J, M\rangle$. The allowed values of the total angular momentum quantum number J satisfy

$$|j_1 - j_2| \;\leq\; J \;\leq\; j_1 + j_2,$$

and for a given J, the magnetic quantum number ranges over $M = -J, \ldots, J$. Both bases span the same $(2j_1 + 1)(2j_2 + 1)$-dimensional Hilbert space.

C.3 Clebsch–Gordan Expansion

The two bases are related by an orthogonal (unitary) transformation. A coupled state $|J, M\rangle$ expands in the product basis as

$$|J, M\rangle = \sum_{m_1, m_2} \langle j_1\, m_1;\, j_2\, m_2 \mid J\, M\rangle \, |j_1, m_1\rangle \otimes |j_2, m_2\rangle, \tag{6.11}$$

where the sum is restricted to terms satisfying $m_1 + m_2 = M$, and $\langle j_1\, m_1;\, j_2\, m_2 \mid J\, M\rangle$ are the Clebsch–Gordan coefficients. Conversely, a product state decomposes

as

$$|j_1, m_1\rangle \otimes |j_2, m_2\rangle = \sum_{J,\, M} \langle j_1\, m_1;\; j_2\, m_2 \mid J\, M\rangle \; |J, M\rangle.$$

Annex D Transient Absorption Spectra Plots

The following figures show the full transient absorption (TA) spectra at selected time delays for each sample and pump-probe helicity combination. Scattering and chirp correction were applied to all datasets prior to analysis.

D.1 R-MBA_2PbI_4

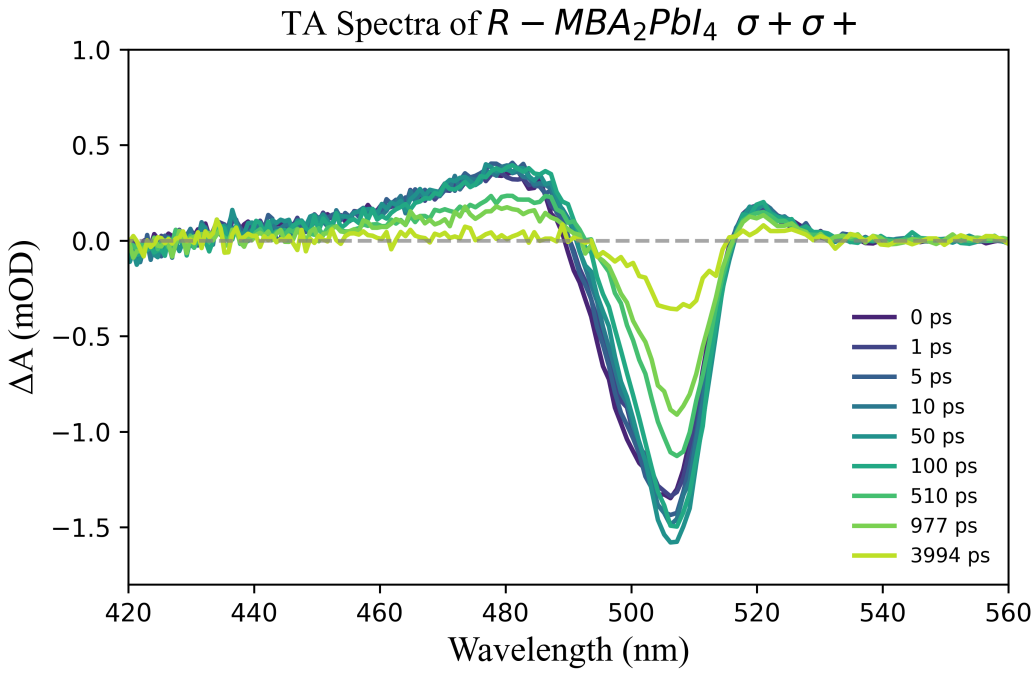

Figure 6.3: TA spectra of R-MBA_2PbI_4 with σ^+ pump and σ^+ probe configuration at selected time delays.

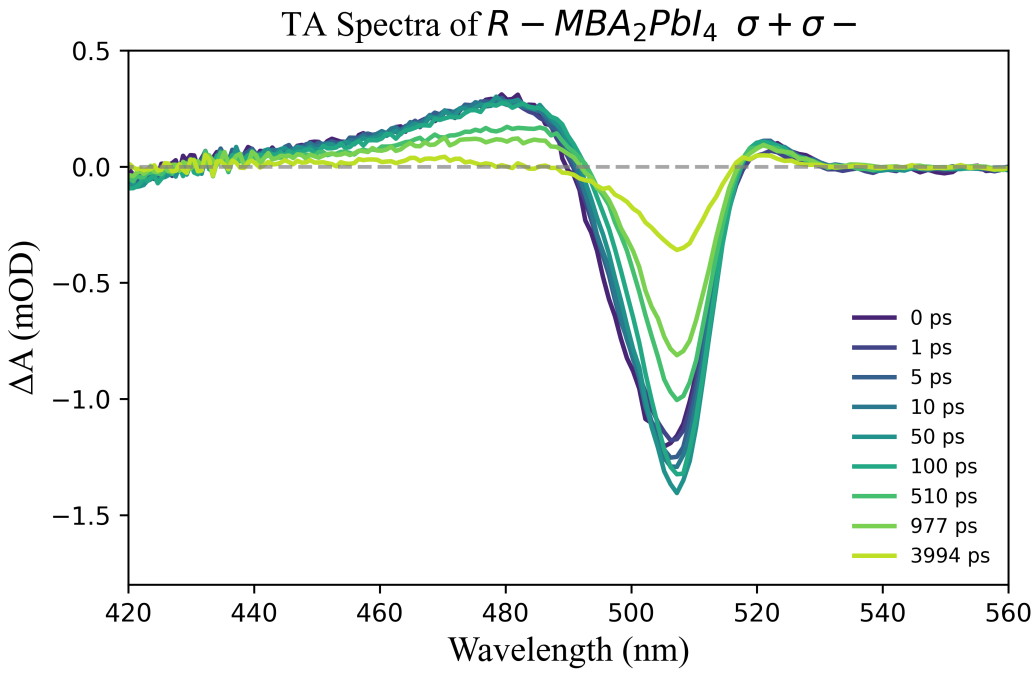

Figure 6.4: TA spectra of R-MBA_2PbI_4 with σ^+ pump and σ^- probe configuration at selected time delays.

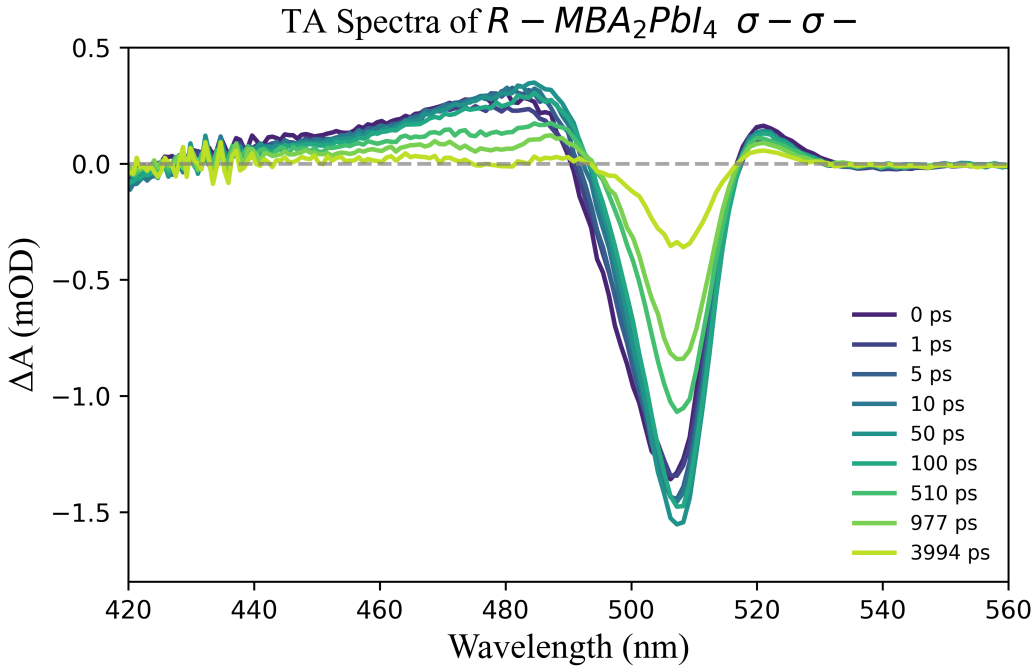

Figure 6.5: TA spectra of R-MBA_2PbI_4 with σ^- pump and σ^- probe configuration at selected time delays.

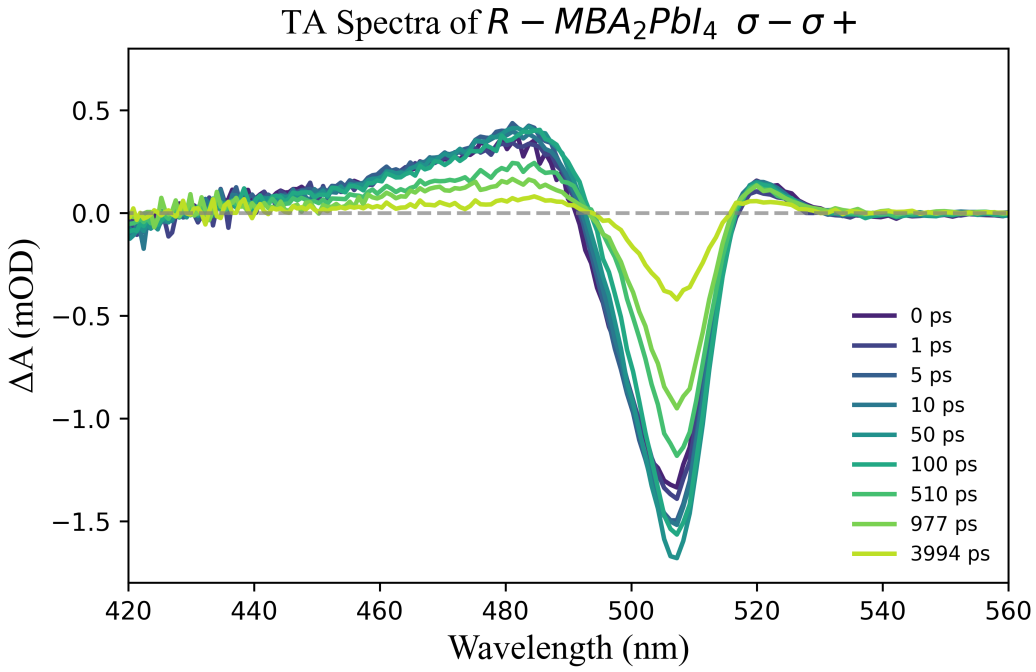

Figure 6.6: TA spectra of R-MBA_2PbI_4 with σ^- pump and σ^+ probe configuration at selected time delays.

D.2 S-MBA_2PbI_4

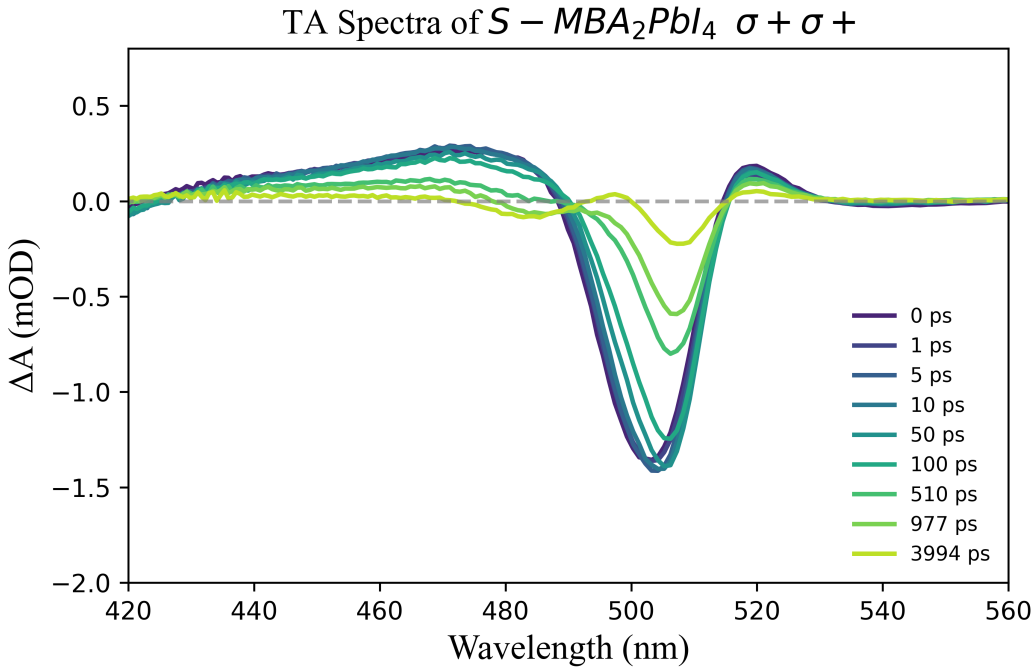

Figure 6.7: TA spectra of S-MBA_2PbI_4 with σ^+ pump and σ^+ probe configuration at selected time delays.

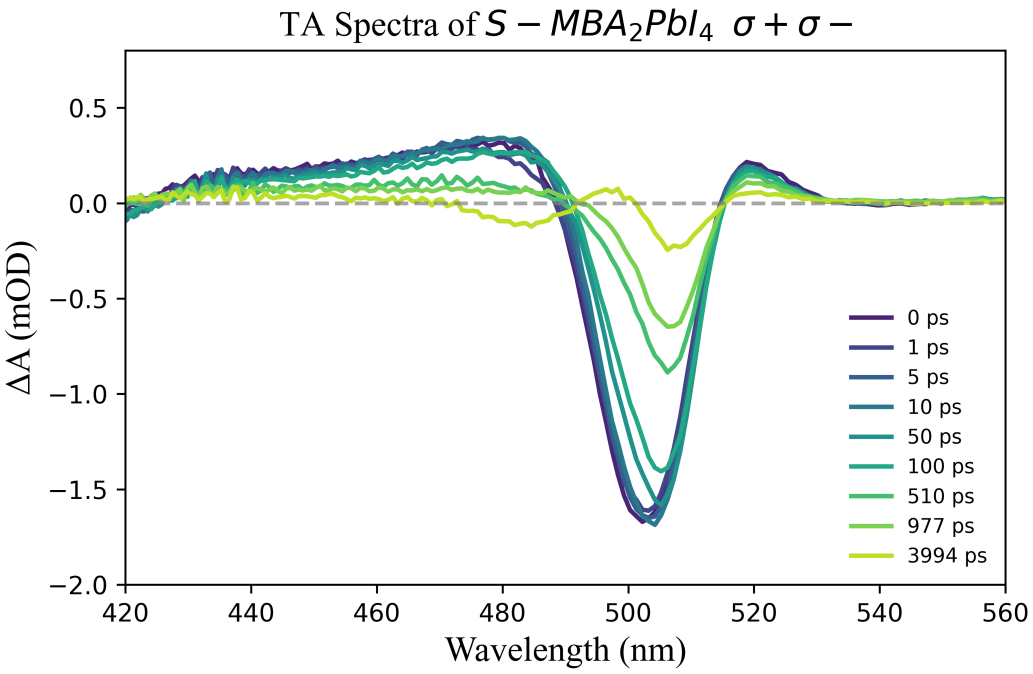

Figure 6.8: TA spectra of S-MBA_2PbI_4 with σ^+ pump and σ^- probe configuration at selected time delays.

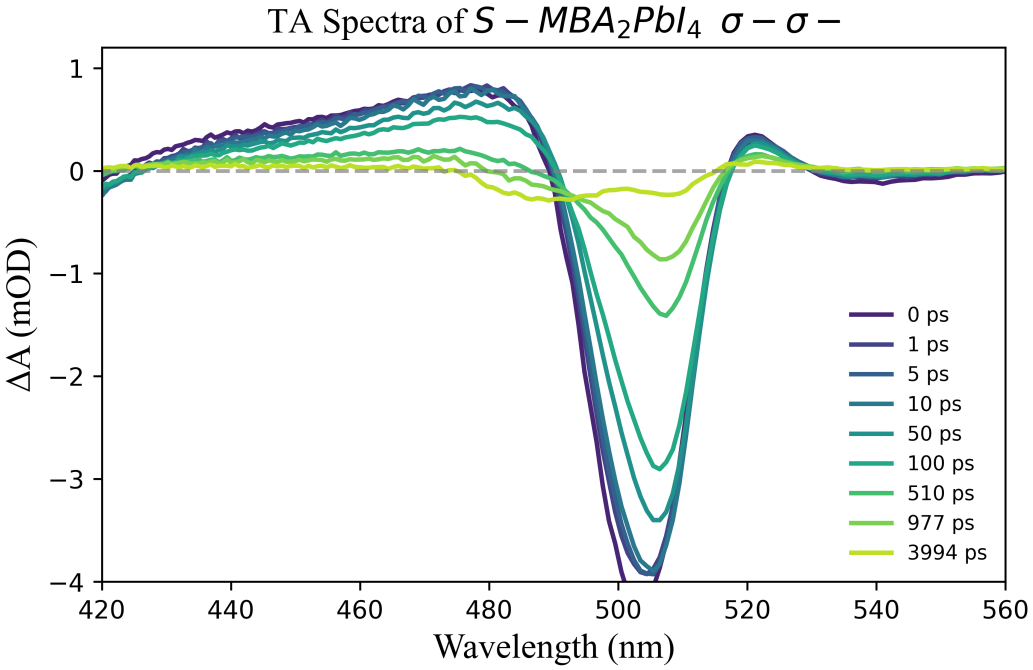

Figure 6.9: TA spectra of S-MBA_2PbI_4 with σ^- pump and σ^- probe configuration at selected time delays.

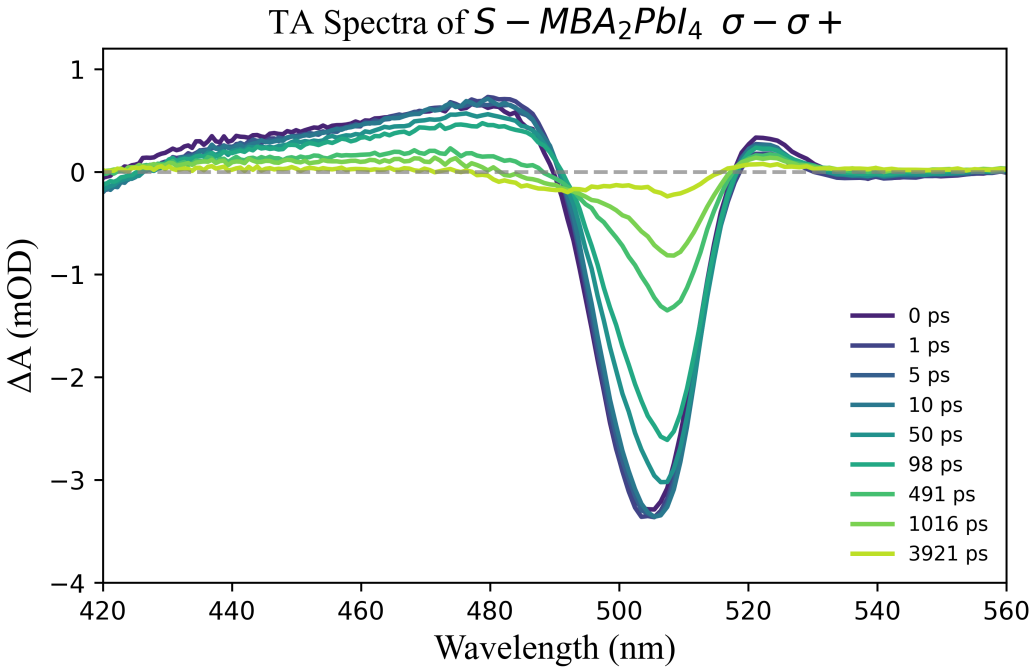

Figure 6.10: TA spectra of S-MBA_2PbI_4 with σ^- pump and σ^+ probe configuration at selected time delays.

D.3 RAC-MBA_2PbI_4

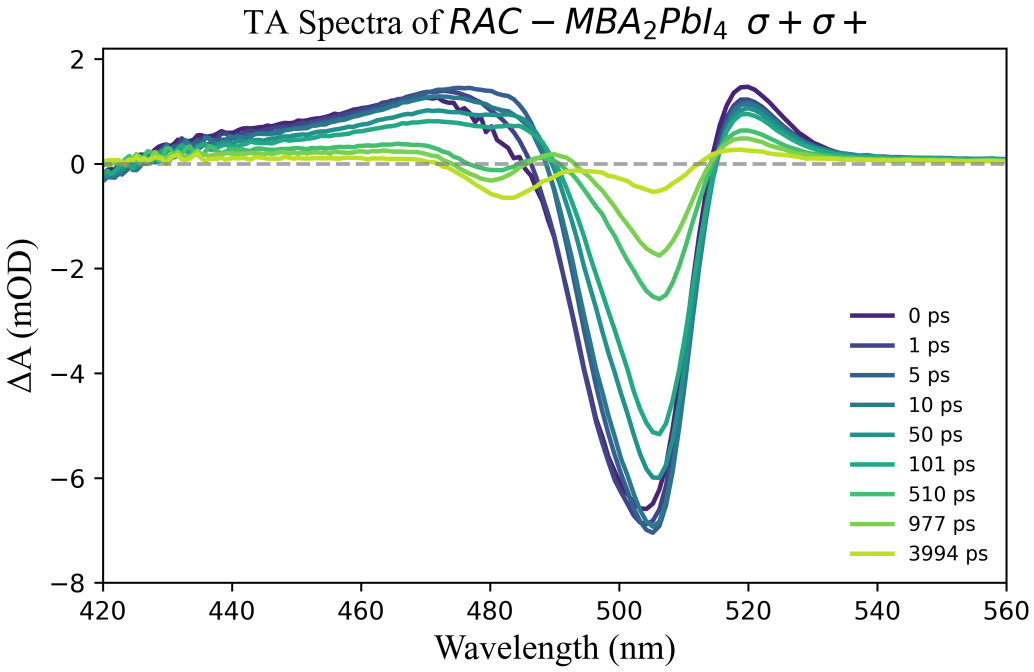

Figure 6.11: TA spectra of RAC-MBA_2PbI_4 with σ^+ pump and σ^+ probe configuration at selected time delays.

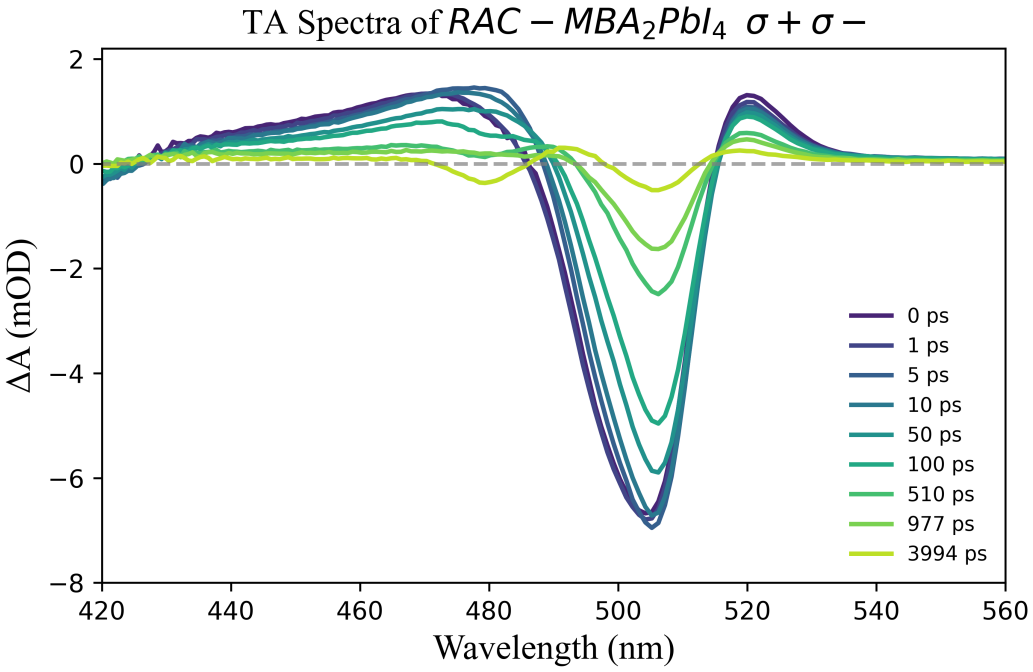

Figure 6.12: TA spectra of RAC-MBA_2PbI_4 with σ^+ pump and σ^- probe configuration at selected time delays.

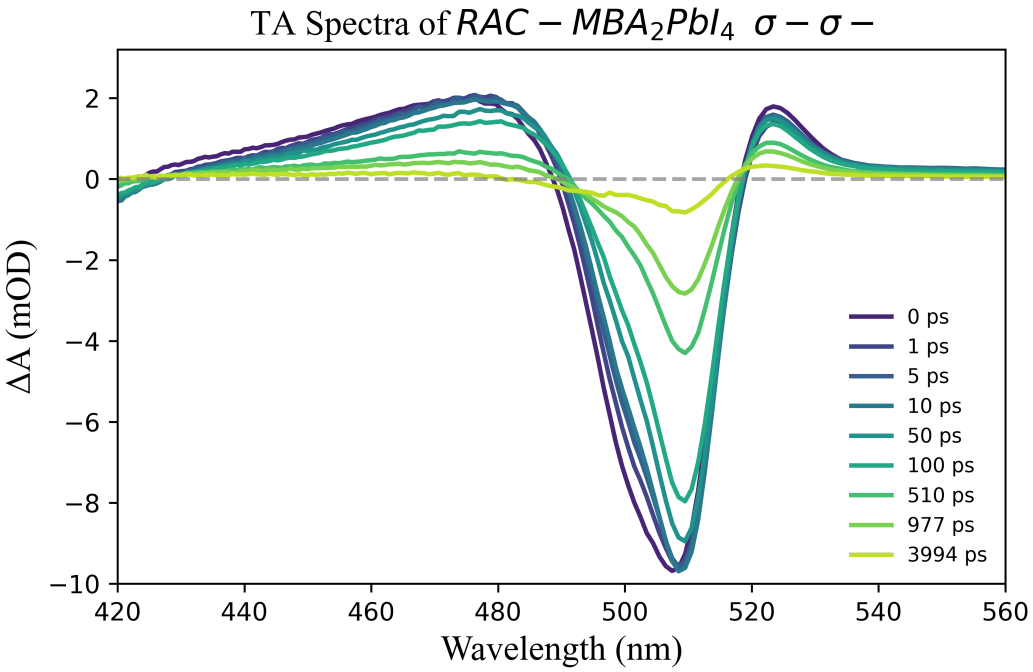

Figure 6.13: TA spectra of RAC-MBA_2PbI_4 with σ^- pump and σ^- probe configuration at selected time delays.

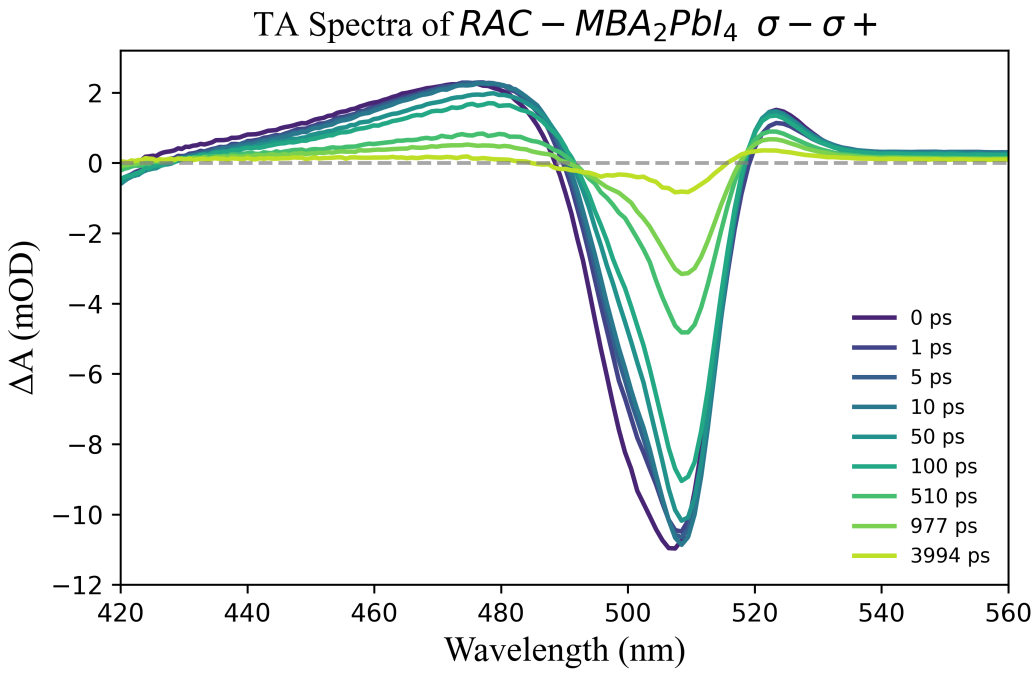

Figure 6.14: TA spectra of RAC-MBA_2PbI_4 with σ^- pump and σ^+ probe configuration at selected time delays.